LAWRENCE
LIVERMORE
NATIONAL
LABORATORY

UCRL-TR-213331

A Non-Interfering Beam Radius Diagnostic Suitable For Induction Linacs

W. E. Nexsen

June 30, 2005

This work was performed under the auspices of the U.S. Department of Energy by University of California, Lawrence Livermore National Laboratory under Contract W-7405-Eng-48.

A Non-Interfering Beam Radius Diagnostic Suitable For Induction Linacs

W.E. Nexsen
Lawrence Livermore National Laboratory
University of California
Livermore, CA 94550

Abstract: High current electron induction linacs operate in a parameter regime that allows the use of a diamagnetic loop (DML) to measure the beam magnetic moment. Under certain easily met conditions the beam radius can be derived from the moment measurement. The DML has the advantage over the present methods of measuring beam radius in that it is an electrical measurement with good time resolution that does not interfere with the beam transport. I describe experiments on the LLNL accelerators, ETA-II and FXR that give confidence in the use of a DML as a beam diagnostic.

I. INTRODUCTION

High current electron linear induction accelerators operate in a parameter regime typically characterized by beam currents in the thousands of amperes, energies as high as 50 MeV, single pulse lengths of less than 100 ns and pulse repetition periods in the seconds or minutes. They are principally used for the generation of flash X-rays and are an important tool of the Safeguard program [1]. Mismatching of the electron beam to its axially symmetric magnetic guide field leads to radial envelope oscillations that can cause emittance growth [2], increase the time averaged spot size and reduce the brightness of the X-ray pulse. The determination of the value of the beam radius at various positions along the accelerator is important when tuning and matching the beam. Presently the basic approach to this measurement is the reduction of images of the light emitted when the beam passes through a thin foil. The measurement integrates over the time that the gated TV camera is recording; if that time is long detail will be lost while if it is short many shots will be needed to study radial variation throughout the pulse. In addition the measurement can only be done at one axial position at a time since the foil perturbs the beam.

In this paper I describe an alternative beam radius diagnostic that is ideal for use on induction linacs. The high beam current, the relatively low beam energy, the guide field strength and symmetry, and the equilibrium beam radius combine to make feasible the time resolved measurement of the beam's magnetic moment by means of diamagnetic loops (DMLs). (In this paper the term DML and "loop" is used interchangeably). Under certain conditions, the beam rms radius can be derived from the moment measurement. Since the diagnostic does not perturb the beam, simultaneous measurement of beam radius at any number of points is possible. In the drift region at the exit of the accelerator, at energies where the beam is emittance dominated, an array of three DMLs located and separated by known beam transport conditions, can, in principle, be used to derive time-resolved single shot measurements of the beam exit parameters-rms radius, slope of the beam envelope, and emittance- and should provide a valuable tool for tuning the accelerator.

DMLs have long been used to measure the perpendicular kinetic energy content of plasmas. Beam connected uses include the measurement of plasma heating by intense electron beams [3], the determination of the angular spread of a magnetized relativistic electron beam [4] and the

measurement of the field of a hollow beam in a field free neutral gas cell [5]. (In the latter case the signal was due to the field and radius at the cathode.) The author is unaware of any attempts to use a DML to measure beam radius in a vacuum prior to 1988 when he began development on this diagnostic on the ETA-II accelerator at LLNL. Encouraging preliminary results were reported in 1991 [6] but no further work was done at LLNL until 1996 when work was resumed at the flash X-ray facility, FXR. (More recently the work was moved back to ETA-II). During the hiatus at LLNL, experimental work was begun [7] and analysis [8]-[9] and computer simulations [10] performed at LANL.

In the main sections of this report we present information of general interest to the reader who might be exposed to the results of DML beam measurements while the appendices give details of interest to those who may desire to implement such measurements. We first discuss the origin of the various components of the beam magnetic moment and the relationship to beam radius. Following this we describe our experimental approach to the moment measurement and finally we present data taken on FXR and ETA-II. The important details of the DML calibration are covered in appendix B and the use of an array to obtain the accelerator output parameters in appendix E.

II. THEORY

When an axially symmetric magnetic field is used to guide a charged particle beam, said beam will have a net azimuthal current component in the diamagnetic direction while in the field. Consequently the beam will have a magnetic moment in this region, defined as

$$M \equiv \pi \int r^2 dI_\vartheta = \pi < r^2 > I_\vartheta \quad . \tag{1}$$

Here I_θ is the aximuthal current per unit beam length. The moment reduces the guide field flux within the beam by the amount

$$\Phi = \mu_0 M \tag{2}$$

A time varying magnetic moment will produce a variation in the flux linking a beam-encircling wire loop and induce a voltage signal across the terminals of the loop. With proper calibration (covered in Appendix B) we can derive the value of the moment from the loop signal and if I_θ is known the rms radius can be obtained using Equation (1).

A. Beam magnetic moment in a totally axially symmetric system.

In an axially symmetric system we can use the principle of conservation of canonical angular momentum to derive the beam rms radius from the loop signal. Canonical angular momentum, which is conserved in an axially symmetric magnetic field, can be written for a beam particle as

$$\begin{aligned} P_\theta &= \gamma(z) m r v_\theta + \frac{q\psi(r,z)}{2\pi} = \text{constant} = \frac{q\psi(r_0,0)}{2\pi} \\ P_{\theta m} &\equiv \gamma(z) m r v_\theta = -\frac{q}{2\pi}[\psi(r,z) - \psi(r_0,0)] \end{aligned} \quad . \tag{3}$$

Here $P_{\theta m}$ is the mechanical component of the angular momentum, $\psi(r,z)$ is the guide field flux linking a circle centered on the field axis and passing through the particle position at (r,z) and $\psi(r_0, 0)$ is the guide field flux at the cathode passing through the point of origin of the particle

now at (r,z). We have ignored the contribution of the thermal azimuthal velocity at the cathode since it is small and averages to zero. Solving for v_θ,

$$v_\theta(r,z) = \frac{|e|}{2\pi\gamma(z)mr}[\psi(r,z) - \psi(r_0,0)] \tag{4}$$

If $j_Z(r,z)$ is the axial current density, the axial current in a shell of radius r, thickness dr is $dI_z = j_z 2\pi r dr$ while the azimuthal current per unit length in this shell is

$$dI_\theta = j_Z(\frac{v_\theta}{\beta c})dr = \frac{1}{2\pi r}(\frac{v_\theta}{\beta c})dI_z \tag{5}$$

and the magnetic moment of the shell is

$$dM = \pi r^2 dI_\theta = \frac{|e|}{4\pi\gamma\beta mc}[\psi(r,z) - \psi(r_0,0)]dI_z \tag{6}$$

From Equations (3), (5) and (6) it follows that

$$\begin{aligned} dM &= \frac{rv_\theta}{2\beta c}dI_z \\ M &= \frac{< rv_\theta > I_z}{2\beta c} = \frac{1}{2\gamma m\beta c} < P_{\theta m} > I_z \end{aligned} \tag{7}$$

The DML diagnostic is unique in its ability to measure the average value of the beams mechanical angular momentum.

Assuming there is no current loss between the cathode and point of observation, the beam moment at z for this axially symmetric case is

$$\begin{aligned} M(z) &= \frac{|e|}{4\pi\gamma\beta mc}[< \psi(z) > - < \psi(0) >]I_z \\ &= M_r(z) - M_c(0) \end{aligned} \tag{8}$$

where

$$< \psi(z) > I_z = \int_0^{R(z)}[\int_0^r 2\pi r' B_z(r',z)dr']\frac{dI_z(r,z)}{dr}dr\,. \tag{9}$$

We note that while $M_r(z)$ depends on the field value in the plane of the loop, $M_c(0)$ is independent of that value, depending only on the field at the cathode, and, with the assumption of no beam loss, the only z dependence in M_c is through $\gamma\beta$.

Where the paraxial approximation can be used to represent the vacuum guide field in the beam region (i.e.,beam radius<<coil radius) and for I<< I_{Alfven}(field depression by the beam is negligible), Equation (9) simplifies to $<\psi(z)>=\pi<r^2(z)>B(0,z)$ and

$$M_r(z)=\frac{|e|B(0,z)}{4\gamma m\beta c}<r^2(z)>I_z=\frac{k_{ce}(z)}{4}<r^2(z)>I_z \qquad (10)$$

Equation (10) is independent of any assumptions about the beam radial profile as long as I<< I_{Alfven}. (For FXR with a maximum current of 4 kA, I/ I_{Alfven}≈ 4% out of the injector and drops to <1% at the accelerator exit).

In the LLNL accelerators, FXR and ETA-II, the cathode is large in radius and the field at the cathode is the algebraic sum of the main injector field and that due to an opposite polarity "bucking" coil behind the cathode. With such a geometry it is difficult to set the field normal to the cathode to zero over the entire surface but by proper adjustment of the bucking coil the current weighted average flux linking the cathode can be minimized. Operationally we set the field at the DML to zero (M_r=0) and adjust the bucking magnet current to minimize the DML signal. Bringing the DML field on then yields a measurement of M_r from which we can derive the rms radius by means of Equation (10) wherever the beam current, beam energy and the magnetic field in the plane of the loop are known.

B. Additional moment components due to symmetry breaking fields.

Section A considers the case of a totally axially symmetric system. In truth at some level no real system is truly axially symmetric as non-uniform emission from the cathode, field errors arising from winding errors in the individual magnets[11] and from tilting and radial displacement of the individual magnets with respect to the accelerator axis, and, possibly, instability driven RF fields break the symmetry and allow transfer of momentum and energy from the axial beam reservoir into the perpendicular components. The common observation of an off-axis helical beam centroid is evidence that such a process does occur. If we can treat the current as concentrated on the beam centroid and if the beam centroid is skew to the axis in the plane of the loop, there will be an additional net flux through the loop. For an isolated circular loop centered on and normal to the axis we show in Appendix A that the net flux due to a skew beam is

$$\Phi=\mu_0 I\frac{\rho\delta}{2} \qquad (11)$$

Here $\rho=\sqrt{x^2+y^2}$ where x, y are the coordinates of the centroid intercept of the loop plane and δ, is the (small) angle between the plane defined by ρ and the axis and the plane defined by ρ and the beam centroid. For consistency with the solenoidal case we define

$$M_\rho\equiv\frac{\Phi}{\mu_0}=I\frac{\rho\delta}{2} \qquad (12)$$

for the case of an isolated loop.

There is one additional possible component introduced by the breakdown of axial symmetry. Equation (12) was derived assuming that the individual particles velocity vectors are essentially parallel to the centroid, thus allowing the current to be treated as concentrated on the centroid. Equation (11) would apply equally well to a current carrying wire filament. The breaking of symmetry means that canonical angular momentum is only approximately conserved and that individual particles, even if born in zero field, may exit the guide field with finite angular momentum and as a result the beam may have a moment component M_u even if the beam is steered to minimize M_ρ. There is no model for this process at present but there is experimental evidence described below of this component.

Experiment suggests that we can assume that all of the moment components except perhaps M_ρ are independent and that

$$M= M_r +M_\rho+M_u- M_c \qquad (13)$$

The additional terms complicate but do not eliminate our ability to determine the beam radius at any given point. Only under certain conditions do they allow us to measure the radius at several locations at the same time, however. For a radius measurement, M_r must be large compared with the sum of the other components in Equation (12). M_ρ can be minimized by steering the beam to the axis in the loop plane while $M_u- M_c$ can be minimized by adjustment of the cathode field with the field at the loop nulled and the beam steered on axis. In this case M_c will no longer be zero but will introduce enough angular momentum to the beam to counter M_u.

III.BEAM MOMENT MEASUREMENT

Since values of beam current and position are needed to reduce the loop data, we have adopted the philosophy of combining all of these measurement into one diagnostic package. Fortunately, this was possible with rather simple modifications of our standard beam current and position monitor. This "beam bug" is a resistive-foil wall-return-current monitor [12]. A coaxial ferrite torus located in a cavity behind the foil increases the inductance of the parallel circuit and forces the bulk of the beam return wall current to flow through a 5μm thick Nichrome foil cylinder whose diameter matches the beam tube and whose length is ~30 mm.

Beam current and centroid position are determined from the voltage drop across the foil measured at eight azimuthally symmetric locations. Signals from four of these voltage pickoff points, 90^o apart, are summed to give a signal proportional to the beam current and insensitive to beam centroid position, while differences are taken of opposing pairs of the remaining four pickoff signals to obtain signals proportional for small displacements to $x*I_Z$ and $y*I_Z$, where x,y are the coordinates of the centroid. Figure 1 shows the modified FXR beam bug incorporating the loop. A cross-linked polystyrene cylinder (Rexolite) is coaxial with and seperates the foil and the ferrite core. O-rings at the cylinder ends form the vacuum seal. One or two turns of 0.018" Formvar insulated copper wire are wrapped and glued in a groove centered on the cylinder .On the time scale of the experiment the beam tube walls force all of the flux perturbations to return within the walls, consequently a loop located at the wall would not detect a signal. The resistive

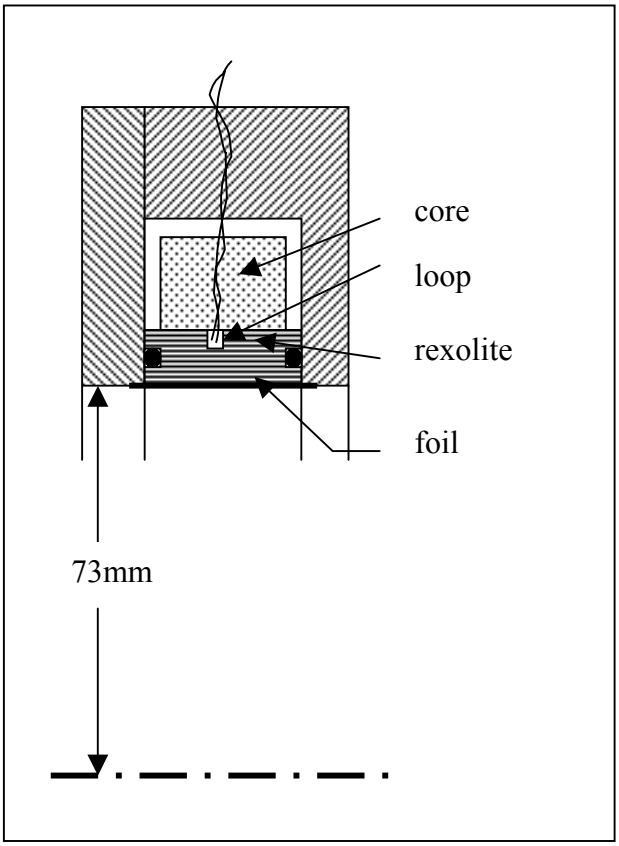

Figure 1 Sketch of FXR beam position monitor modified for loop

foil is much thinner than the skin depth for frequencies of interest, however, and flux can penetrate the foil. The ferrite cavity behind the foil allows some axial flux to return external to the loop, with the result that a net flux links the loop. The foil cylinder acts as a L/R integrator of the primary beam signal, distorting the loop signal but a wide bandwidth replica of the true signal can be recovered with the aid of algorithyms described below. Further DML design details and suggestions for improvement are given in Appendix F. While our design approach gives a signal strength appreciably less than that from a smaller diameter loop mounted inside the beam tube, the signal strength is sufficient for satisfactory recording and our signal to noise ratio may be better. The foil configuration as well as the position of the eight voltage pickoffs was unchanged by the modifications to the beam bug. Consequently the current and position calibrations were unchanged.

This approach to the loop design has a number of advantages:

- The beam tube bore is kept clear and unchanged.
- No additional axial length is required for the diagnostic.
- Beam bug modifications are relatively simple
- Beam current and position are measured at the loop plane
- The foil terminates and shields the loop from B_θ
- The loop is electrostatically shielded.

In our design the loop links both the beam and the beam bug foil, consequently the signal it detects is due both to the beam and to the azimuthal currents induced in the foil by the beam. Initially the beam moment will be cancelled by the foil moment and no signal will be observed. With time the induced foil current will decay off because of the foil resistance, flux will penetrate the foil and loop signal will be induced. The relation between the beam moment M(t) and the loop signal V(t) is given by

$$M(t) = k[\frac{\tau_2}{\omega^2}\frac{d^2V(t)}{dt^2} + (\tau_1\tau_2 + \frac{1}{\omega^2})\frac{dV(t)}{dt} + (\tau_1 + \tau_2)V(t) + \int_{-\infty}^{t} V(t')dt'] \qquad (14)$$

Here k is the calibration constant, τ_1, τ_2 are related to the loop and foil L/R time constants, while $1/\omega^2$=LC where L is the loop inductance and C is the parasitic capacity of the loop leads. The values of these parameters are obtained from the loop calibration described in Appendix B.

III. LOOP TESTS ON FXR AND ETA-II

A. Cathode field optimization.

If the local field at the DML can be set to zero without loss of beam current, and the beam steered to pass through the loop plane on axis, any remaining DML signal can be minimized by adjustment of the field at the cathode. In FXR this field is the sum of the contributions of five coils. Four of these, designated I21, I22, I23, I24, are downstream from the cathode and are the first magnets of the main guide field while the fifth, I20, located slightly behind the cathode is a larger diameter "bucking" coil, normally run at opposite polarity to control the field at the cathode. In the runs described below we varied only the current in I20 while leaving the remainder set to their tune values. We expect the measured moment per unit current to vary linearly with the current in the bucking coil, passing through zero and changing sign for some value. This will be the optimum setting for the bucking coil current.

The results of three scans taken on different days with the same tune are shown in Figure 2. The plotted points are the average values of M/I during a 20 ns period around the beam current peak. The data was taken in the drift region at the exit of the accelerator using one DML for the data of 6-27-03 and a second , downstream and separated from the first by a drift space, for the other two dates. For each run the field at the pertinent DML was zero. For reference the average cathode flux is zero for a bucking coil current setting of about 150A. The difference between this value and the null value of 207A from 1-9-04 corresponds to a cathode field value opposite to the main field of almost 30 gauss.

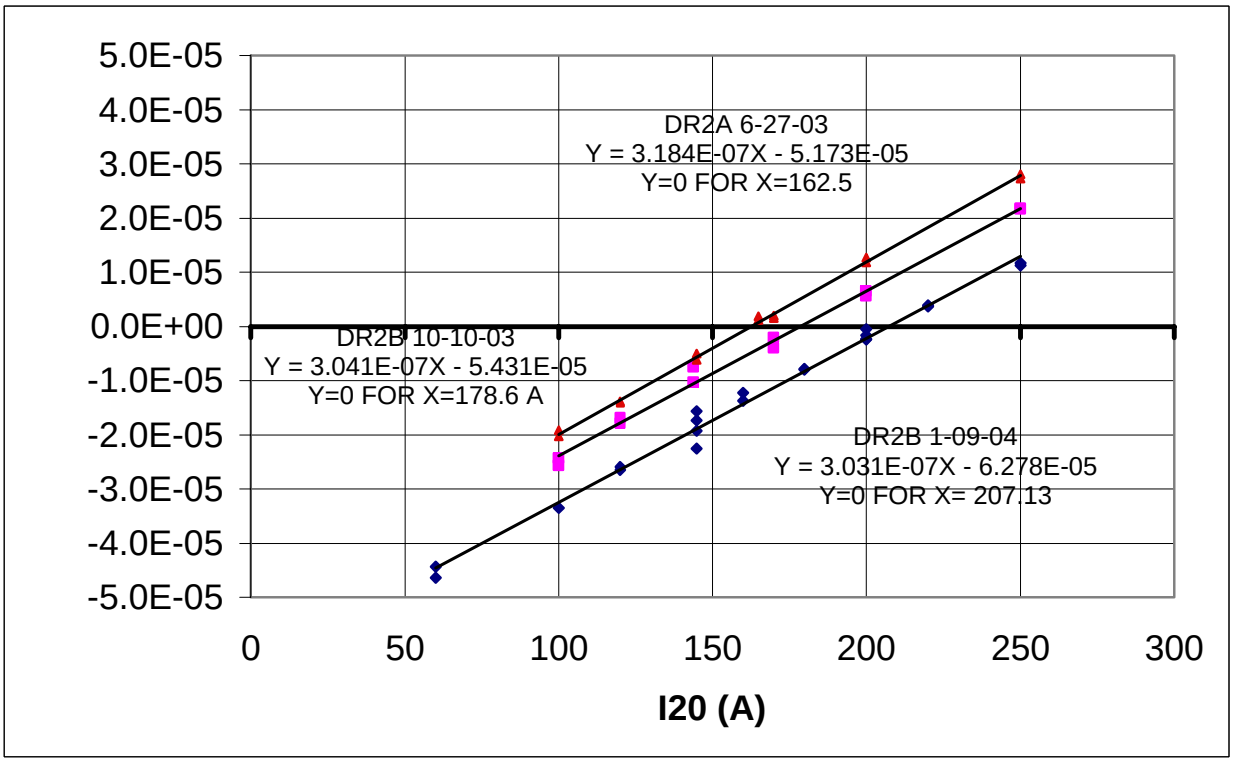

Figure 2. Average values of M/I at FXR exit versus bucking coil current for three different days.. Tune REX02E.

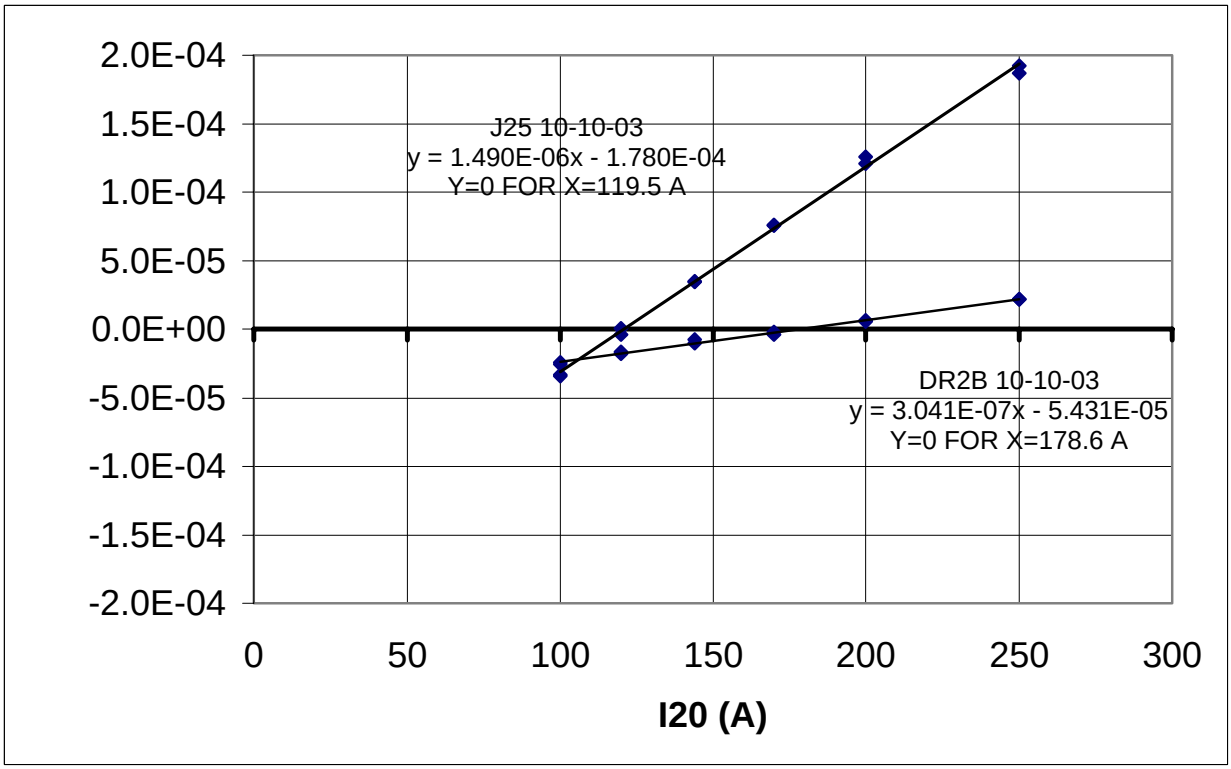

Figure 3. Overlay of M/I versus bucking coil current at two locations .

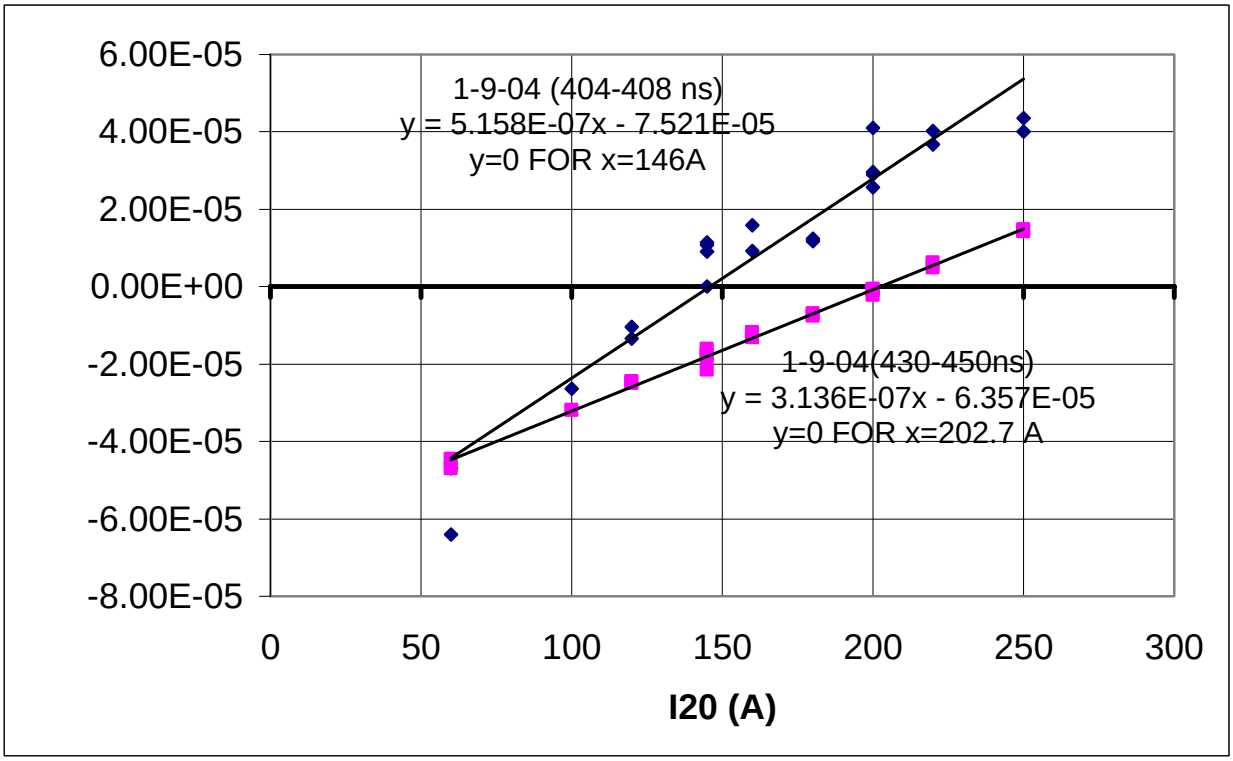

Figure 4. Overlay of M/I over two different time intervals versus bucking coil current.

Further light may be shed by Figure 3 where the above data of 10-10-03 is over-laid with data taken on the same day and with the same tune with a DML located one cellblock downstream from the injector. The difference in slopes reflects the difference in beam energy at the two locations. Notable is the difference in values of I20 current for nulls at the two locations, a total separation of almost sixty amperes almost evenly spaced around the null flux value of about 150 A. This data disputes any hypothesis that the shifts are due to a calibration or power supply error but may be evidence that the shifts are energy sensitive. This is further illustrated in Figure 4 where the data points of a 20 ns average around the current peak overlays points averaged over a 4 ns interval early in time when the current is rising rapidly. The larger scatter in the latter set is probably due to the smaller time interval during which signals are changing rapidly. The difference in slopes indicates that the average value of γ during this time is about 0.6 of the peak value.

This variation of the value of the bucking coil current value for which <M/I>=0 is evidence that in FXR the canonical angular momentum of the beam is not conserved. Such variation had been noted a number of times in the past but had been assumed to be due to the contribution of a skewed beam. On 1-09-04, however, I used the two drift region beam bugs, separated by a 1.054 m drift length, to measure both δ and ρ simultaneously. The beam was steered to reduce the centroid displacement from the DML center to the order of a millimeter while δ was determined to be of the order of a few milliradians. These values in Equation 12 yield a very small correction to the measured moment and a shift of only a few amperes of bucking coil current for the null. This is shown in Figure 5. The skew model alone cannot explain the observed value of the beam moment in the drift when the current weighted average flux at the cathode is zero.

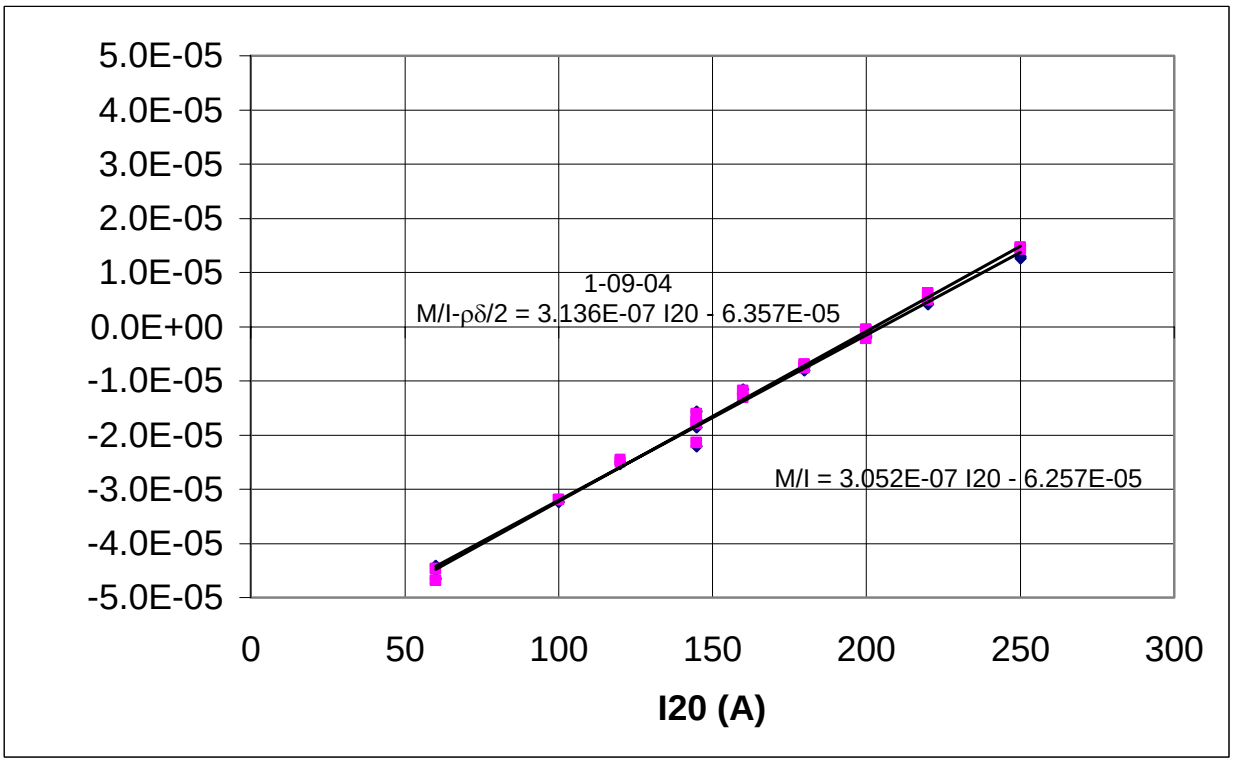

Figure 5. Overlay of bucking coil scan skew centroid model correction.

The results of the bucking coil scans fit the relationship

$$M/I_z = -\frac{1}{4\pi}\left(\frac{|e|}{\gamma m\beta c}\right) < \Psi(0) > + (M_u/I_z) \qquad (15)$$
$$= (< P_{\theta m} >_c + < P_{\theta m} >_u)/2\gamma m\beta c$$

where the first term on the right is the contribution to the azimuthal mechanical momentum of the cathode flux while the second term on the right is the result of the breaking of axial symmetry which introduces torques on the beam. The two terms at this level of approximation are independent and additive. Why the second term varies from day to day for supposedly the same operating conditions is a matter for study and conjecture. We do know that small changes in beam energy produce the "corkscrew" motion of the beam centroid and that this varies from day to day. Perhaps the second term is controlled by the phase of the helical centroid as it encounters the various error fields and steering fields.

In any case individual beam particles have acquired additional angular momentum in their passage through the machine that does not disappear when they exit the machine. It is of course true that even in an axially symmetric system the individual particles will have some angular momentum upon exit if the field is not zero everywhere on the cathode, but their contribution averages to zero if the current weighted average flux at the cathode is zero. An important question is whether the beam simply gains rotational momentum without spreading, or does some of the momentum gain randomize? (Figure 6) The first option seems too good to be true and is certainly a violation of Murphy's Law. In this case we would only need to adjust the bucking coil to a value for which the rotation was canceled at the target. Alternatively, through mechanisms at present unknown but certainly involving the breakdown of axial symmetry the distribution may have spread.

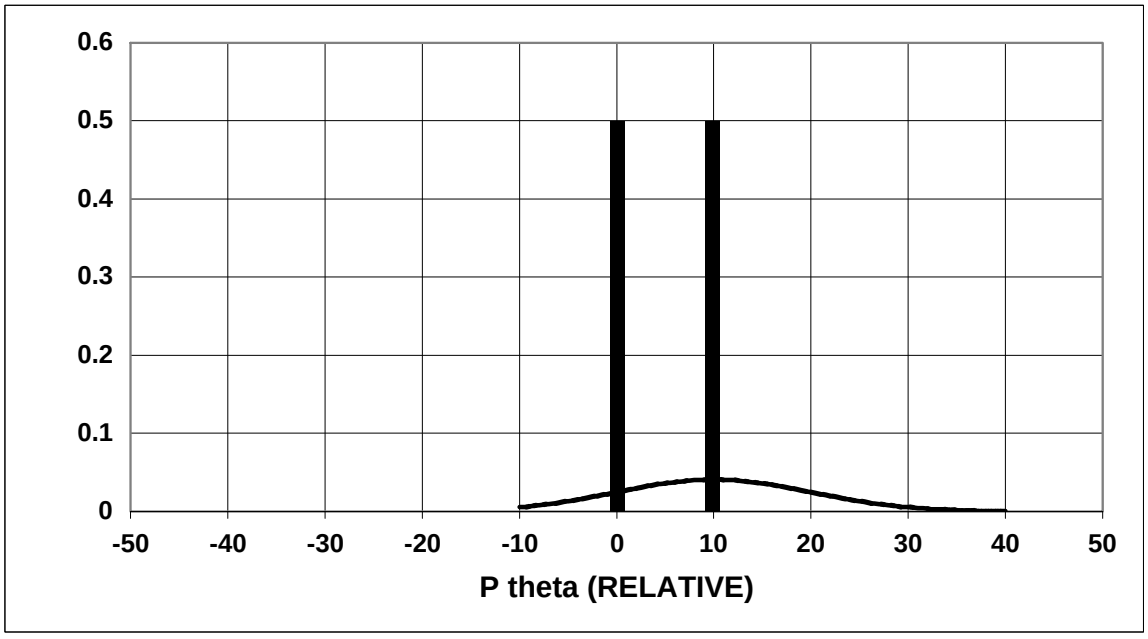

Figure 6. Two models for the gain in azimuthal momentum.

If we approximate the spreading by a normal distribution with standard deviation, σ, the effective un-normalized rms emittance will be

$$\varepsilon = \sqrt{\varepsilon_0^2 + < P_{\theta m}^2 > / (\gamma m \beta c)^2}$$
$$= \sqrt{\varepsilon_0^2 + (\sigma^2 + < P_{\theta m} >^2) / (\gamma m \beta c)^2} \qquad (16)$$
$$= \sqrt{\varepsilon_0^2 + (\sigma / \gamma m \beta c)^2 + (M / I_z)^2}$$

Can this be the explanation for the large FXR emittance? For the bucking coil set to its tune value, the largest value of M/I_Z of Figure 2 is about 2E-5 for the data of 1/9/04. In emittance units this is 2 cm-mr, certainly much smaller than the values of about 10 cm-mr measured by OTR and DML. To explain the measured emittance values by this process alone would require that the standard deviation of the spread distribution be of the order of five times the average value.

B. Experimental test of loop calibration

From our knowledge of the field at the cathode and beam energy and current at the loop we can calculate the expected value of the moment and compare with its measured value to check the calibration and the validity of the assumptions leading to Equation (15).The data reported above was taken with the AK gap set to 120 mm for which the field on axis of the FXR cathode is given by

$$B(0,0) = 0.180 I_{21} + 0.033 I_{22} + 0.030 I_{23} + 0.021 I_{24} - 0.487 I_{20} \text{ (gauss)} \qquad (17)$$

where $I_{20}, I_{21}, I_{22}, I_{23}$ and I_{24} are the currents in amperes in coils I20, I21, I22, I23 and I24 respectively. . The radial variation of the field at the cathode is close to parabolic,

$$B_z(r,0) \approx B(0,0) + \Delta B (\frac{r}{R})^2 \qquad (18)$$

where R is the radius of the cathode, and the radial variation of the flux at the cathode is

$$\psi(r,0) \approx \pi [B(0,0) r^2 + \frac{\Delta B}{2} \frac{r^4}{R^2}] \qquad (19)$$

Since the cathode is located in the fringing field of I21 and I22 while it is located close to the plane of the larger diameter I20, we can assume that ΔB is mainly due to I21 and I22, and that varying the current in I20 will have little effect on ΔB which was measured to be about –4.5 gauss for the tune values. We use the model profile for the current emitted from the cathode,

$$J_z(r,0) = \frac{I_z}{\pi R^2 (1 + \nu/2)} (1 + \nu \frac{r^2}{R^2}) \qquad (20)$$

where ν is the shape parameter, -1≤ ν. For ν = 0, the profile is flat while if ν = -1, the profile is parabolic and for ν = 1 the profile is somewhat hollow. This distribution gives for the current weighted average of the cathode flux,

$$< \psi(0) > = \frac{\pi R^2}{2 + \nu} [(1 + \frac{2}{3} \nu) B(0,0) + (\frac{1}{3} + \frac{\nu}{4}) \Delta B] \qquad (21)$$

and

$$(\frac{M}{I})_{calc} = -\frac{1.76E07 R(0)^2}{4(2 + \nu) \gamma \beta c} [(1 + \frac{2}{3} \nu) B(0,0) + (\frac{1}{3} + \frac{\nu}{4}) \Delta B] \qquad (22)$$

when B is in gauss. The data above was taken with the injector magnets set to the tune values, I_{21} = 295 A, I_{22} = 483 A, I_{23} = 109 A and I_{24} = 63 A. We use these settings in Equations (17) and (22) to obtain the calculated value of M/I as a function of the bucking coil current for γ=34, ν=0 and1. The beam from the cathode would be expected to be somewhat hollow and the correct values of

$(\frac{M}{I})_{calc}$ should lie somewhere between ν=0 and ν=1 The measured values of M/I are plotted against the calculated values in Figure 7 for the two values of ν and the linear fits of these data superimposed. They show a relationship given by

$$(\frac{M}{I})_{meas} \approx (\frac{M}{I})_{calc} - Constant \qquad (23)$$

The possible origin of the constant term has been discussed above. The slope close to unity promotes confidence in the DML calibration process. FXR is not equipped with a beam energy

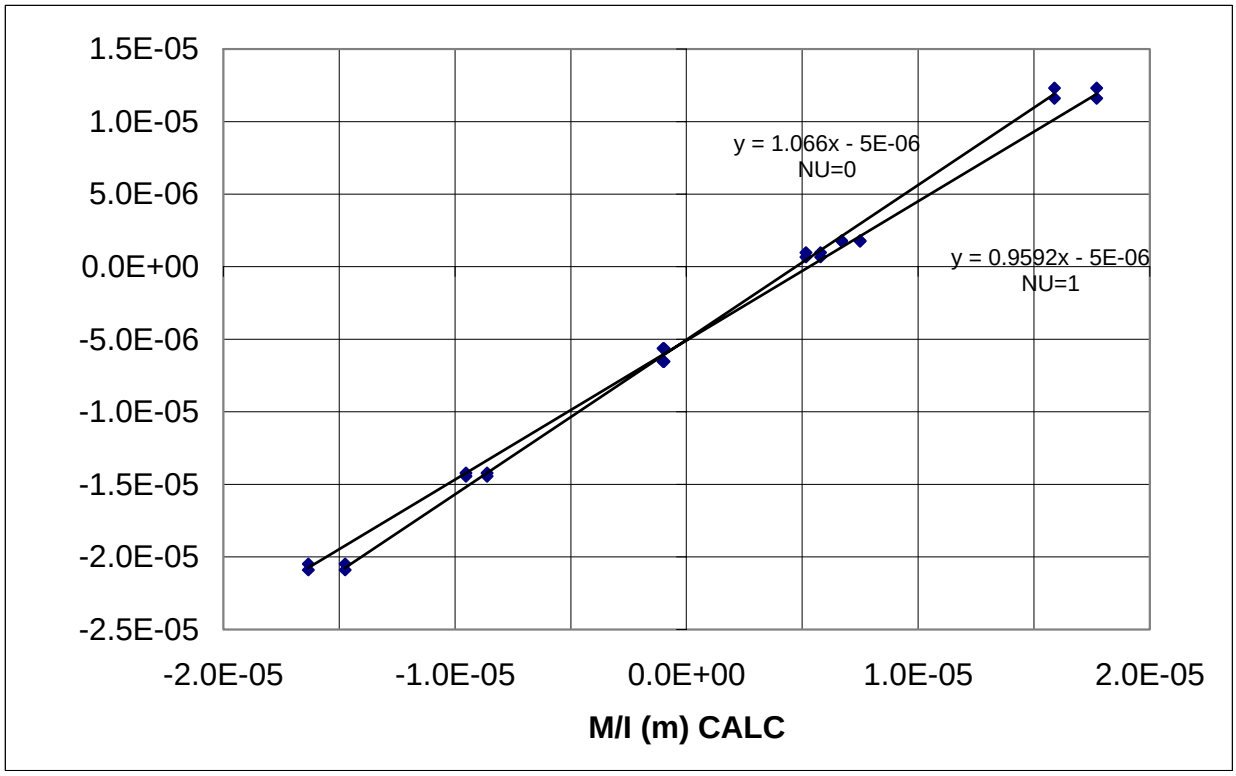

Figure 7 Measured M/I versus calculated M/I for ν=0,1 and γ =34.

analyzer and the most important source of error in the calculated M/I is the value of the beam energy that is based on cell voltage measurements. This estimate is probably good to ± 5% and all other sources are believed to be small compared with this. The experimental values depend on the loop and beam bug current calibrations. In light of these uncertainities the agreement between expected and measured values is remarkable and, while one can not dismiss the possability of offsetting systematic errors, invoking Ockham's razor leads to the□□□ conclusion that the uncertainites in the loop measurement of beam magnetic moment are small. At present we cannot differentiate between a constant current radial distribution at the cathode and the slightly hollow distribution that theory predicts.

C. Comparison of DML and foil beam radius measurements.

In the present generation of induction linacs the beam radius is obtained usually by reduction of the image of the light produced when the beam strikes a thin foil. Here we compare such a set of data with those obtained from simultaneous DML measurements of beam radius. The measurements were made downstream of the ETA-II accelerator exit in the beam transport

region that consists of a series of short-solenoid lenses separated by long drift spaces. The DML was located in the fringing field of one of these lenses, labeled EF1 while the foil was located in a cross 41 cm downstream from the DML. Except for several shots at the beginning and the end of the run when the current in EF1 was set to zero, the EF1 current was kept at a constant value of 7 A which gave a DML bias field of 139 Gauss while the beam radius was varied by adjusting the current in the next upstream solenoid, EF0. At the beginning of the run the ETA energy analyzer measured the beam total energy at 5.39 MeV at the time of peak current. (Peak current was slightly less than 2kA.) Since it was not physically possible to make the two radius measurements at the same location, the beam entrance conditions into the transport region that

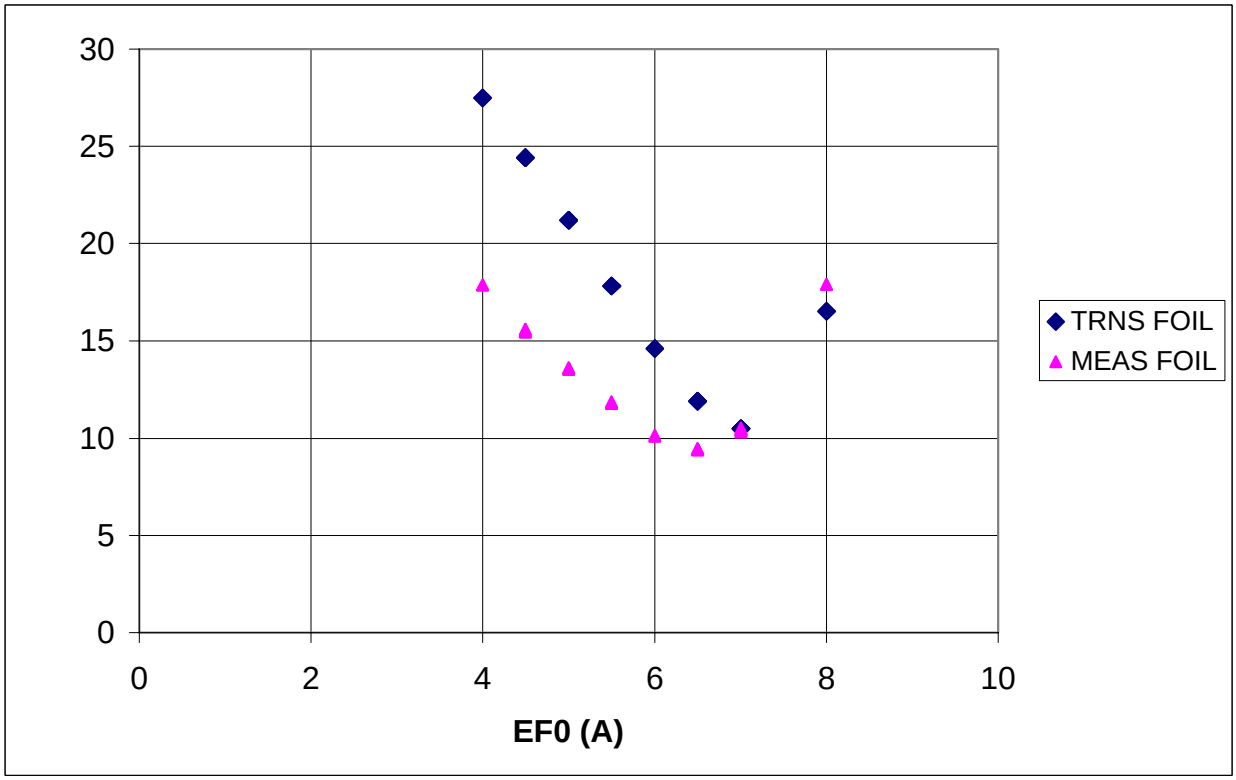

Figure 8 Foil measurements of rms beam radius and implied values at DML.

best fitted the foil data was determined, yielding R= 7.9 mm, R′=3.5 mr, emittance=5.1 (cm-mr), current =1800 A and kinetic energy= 5.25 MeV. These values were then used to determine a consistent set of "foil" radii at the DML position. The beam radii as measured at the foil and the implied values at the DML as determined from the FITS code are plotted in Figure 8 as functions of current in EF0.The conditions of this scan had been repeated twice previously at which times only the M_r component was found to be important but for this days data it was found, after the fact, that the moment measured with zero DML field, M_0, was large enough that it was necessary to correct the moment measured with field on, M_B. We set $M_r = M_B - M_0$ where M_0 was taken as the average value over 10 ns at peak current of four shots, two at the beginning and two at the end of the run. In Figure 9 we plot the uncorrected and corrected DML radius measurements. The numbers by the uncorrected points are the shot numbers and illustrate the reproducibility of the measurements. In the case of theEF0= 6.5 and 7 A data adjacent shots overlay but diverge from values from later in the run indicating some change has occurred in the operation. Finally in

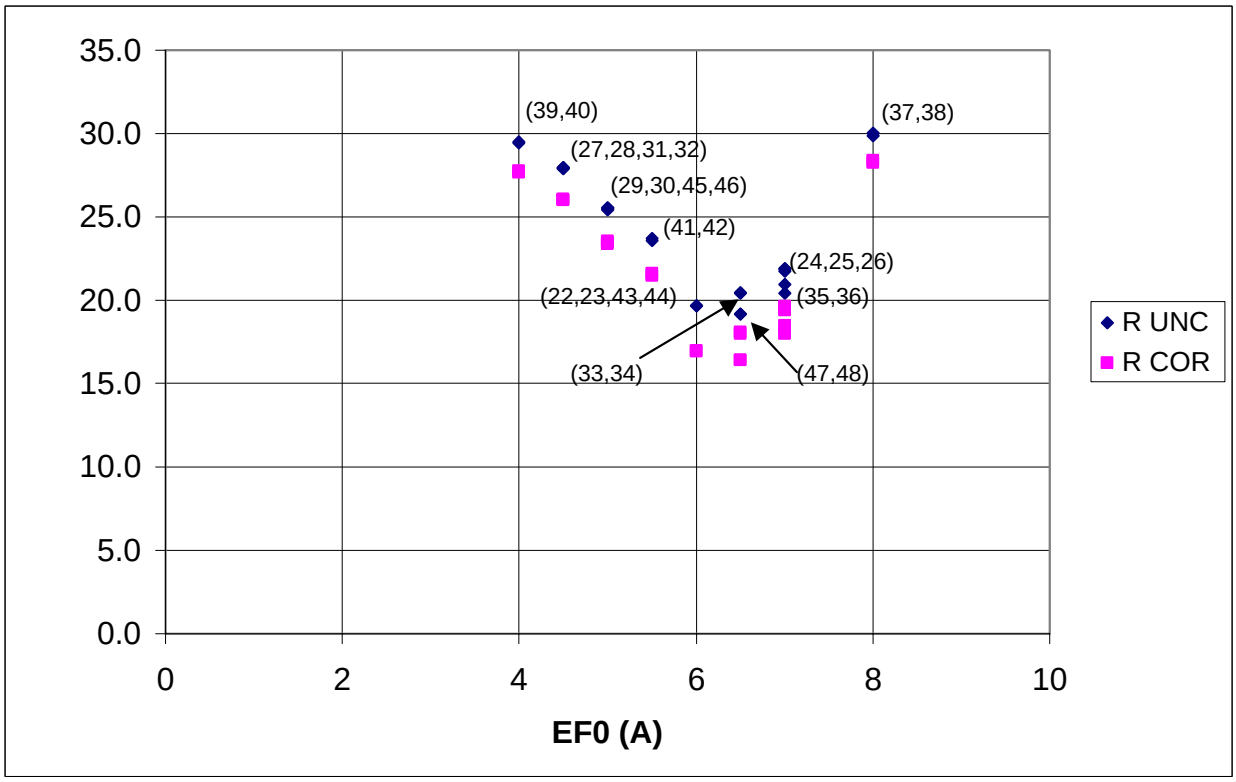

Figure 9 Uncorrected and corrected DML rms beam radius measurements.

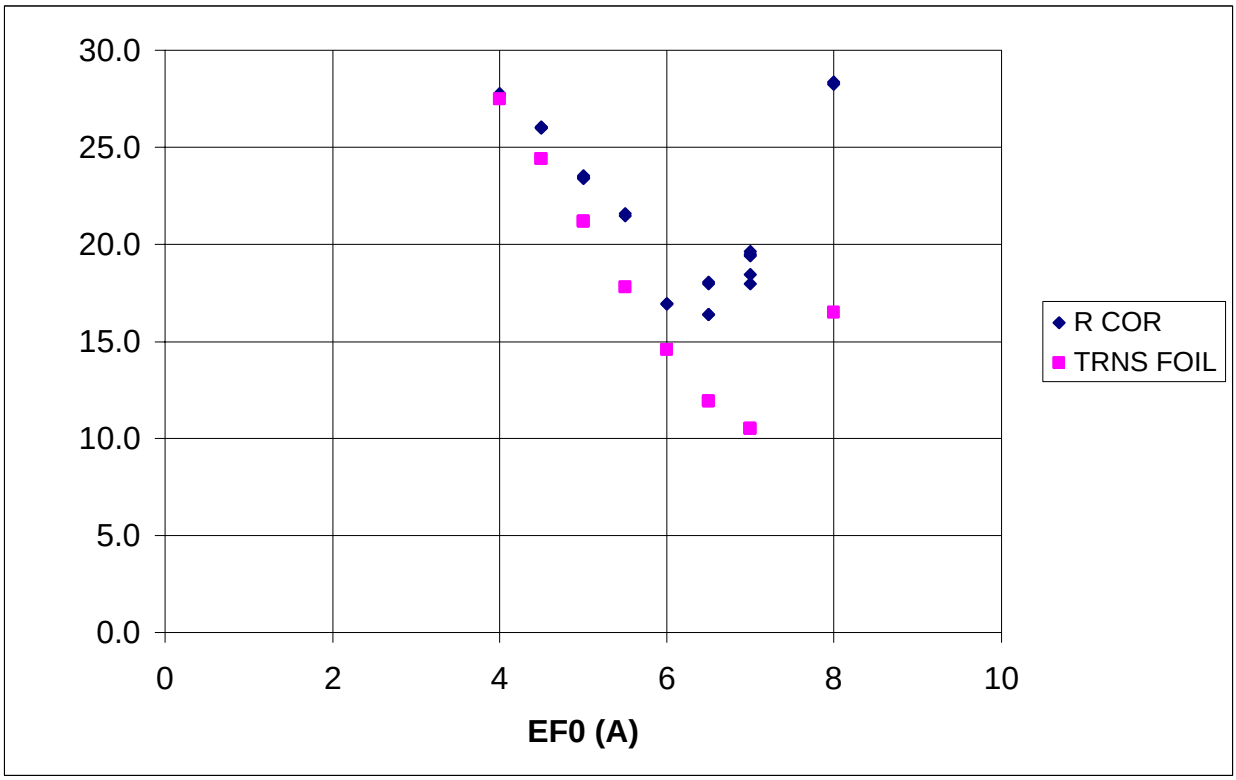

Figure 10 DML and foil measurements of beam rms radius.

Figure 10 we plot the implied beam radius at the DML from the FIT treatment of the foil data and the corrected DML measurement. The two measurements agree at EF0=4A but diverge at higher values. Especially noticeable is that the EF0=8A DML value obtained from the next two shots after the EF0=4A measurements is almost the same as the latter value and is certainly as good as that measurement. This may indicate some error in the FIT values used to generate the implied foil values as does the fact that the minimum radius for the two sets of measurements occur at different values of EF0 current.

I argue that both of these sets of measurements are valid and diverge because they are measuring two different parameters. The DML yields a rms radius for the total beam passing through the loop and is independent of any assumptions about the radial profile of the beam. The foil measurement concentrates on the core of the beam and through the choice of a baseline before reduction ignores the contribution of any very low level halo that might be present. We illustrate this difference by invoking a crude model current distribution. Assume a radial distribution given by

$$\begin{aligned} f(r) &= 1 && 0 < r < r_0 \\ &= \delta(r_0/r) && r_0 \le r \le R \end{aligned} \tag{24}$$

where δ is some small fraction of the peak density at r_0 and R is the radius of the beam tube wall. This distribution has a rms radius given by

$$R_{rms} = \left(\frac{(r_0 R^3/3)\delta + (1/4 - \delta/3) r_0^4}{r_0 R\delta + (1/2 - \delta) r_0^2} \right)^{1/2} \tag{25}$$

The DML would be expected to yield this radius; the foil measurement, if δ is so small as to

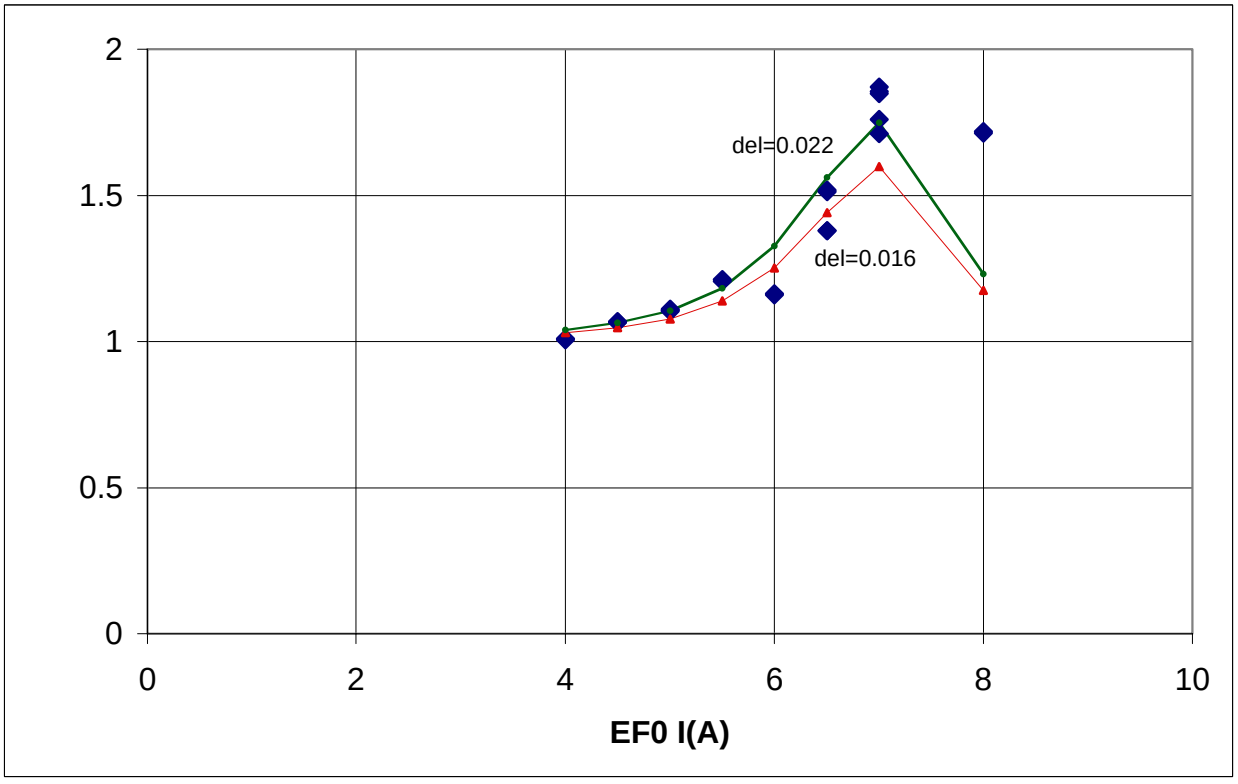

Figure 11 The ratio of the two data sets overlaid with Equation 26 values.

be ignored, will give $r_0/\sqrt{2}$ and the ratio of the two measurements is

$$\text{Ratio} = \frac{\sqrt{2}}{r_0}\left(\frac{(r_0R^3/3)\delta + (1/4 - \delta/3)r_0^4}{r_0R\delta + (1/2 - \delta)r_0^2}\right)^{1/2} \qquad (26)$$

In Figure 11 we plot the ratio of the corrected DML rms beam radius measurement to the implied foil rms radius, i.e., the data plotted in Figure 10. Also shown are the ratio values from Equation 26 for two values of δ, for the beam tube radius, R=66 mm and $r_0=\sqrt{2}$ times the implied foil rms radius at the DML, Although this model is crude it illustrates that a halo with current density at the edge of the main distribution of the order of 2% of the peak density can explain the divergence of the two sets of measurements.

Several other sources provide evidence of the existence of a halo:

- The DML can act as a probe that detects beam electrons hitting the walls.
- Current is lost between the DML and the next downstream beam bug.

The signals from the two DML terminals, designated A and B, have been recorded separately. Their difference, B-A, is the voltage induced by changing flux linkages while, if the loop is floating, any resultant B+A signal indicates a net charge entering the loop. The ETA measurements have shown the presence of such a signal, negative in polarity signifying a net influx of electrons into the loop. Whether these are secondary electrons produced by direct bombardment of the DML surroundings by energetic beam electrons or whether there is an intermediate stage involving x-rays is not known at present. The data considered above was taken with a loop whose center point had been grounded, allowing any charge to be bled off but similar runs had been made earlier with an ungrounded loop and the A+B data from one such run is shown in Figure 12. This data was taken under the same conditions of EF1=7A and EF0 varied

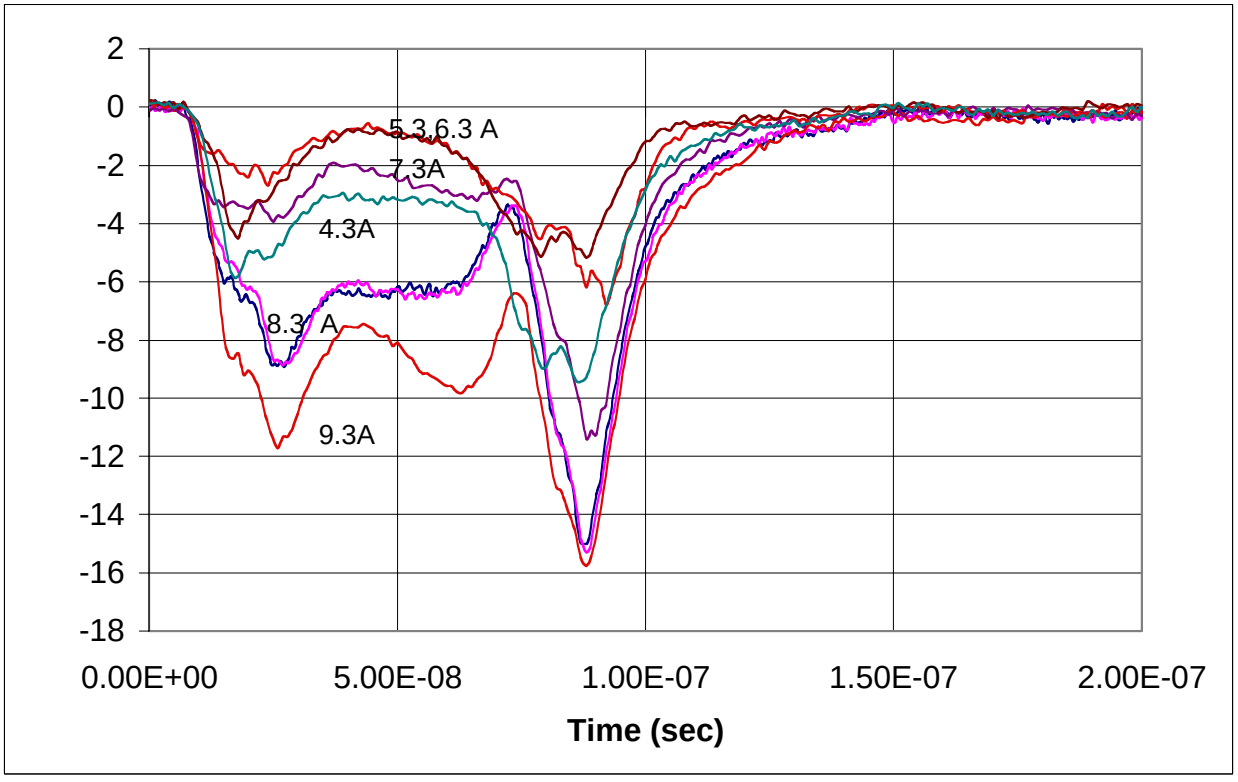

Figure 12 A+B data from 9/3/04. EF1=7A. Labels are EF0 current values.

and shows a signal occurring when beam is present, whose shape and magnitude depend on the value of current in EF0 and thus on the size of the beam at the DML. Observe that the signals have a minimum for values of EF0 in the same neighborhood as the minimum in radius. We interpret these signals as evidence that there is a beam component in contact with the wall at or near the DML.

If the beam-bug calibrations could be believed there would appear to be on the order of a minimum 70 A loss of beam current between the DML and BBT05, located 22.1cm downstream. We know from experience, however, that such a loss is suspect, probably because the beam-bugs are not calibrated with the summing chassis they use on ETA. Also from experience we know that when current is lost, it usually is lost over only a portion of the signal profile, consequently if by scaling one of the beam-bug calibration constants we get a good overlay of the two signals we can rather safely assume that there is little current loss between them and choose the scaled value as the correct calibration relative to the first beam-bug calibration. Subsequently if we no longer get a good overlay under a different running condition we can interpret this as being due to current loss between the two beam-bug position. We illustrate this in the next several figures. In Figure 13 we plot a condition from our DML-foil data set for which we get our best overlay. This is for EF0 set to 5.5 A and with the BBT05 calibration increased from 212A/V to 218A/V or about 3% while the DML calibration was kept constant at 198 A/V. While this seems to be the best eyeball fit, the current, when averaged over a 10 ns period around the peak current,

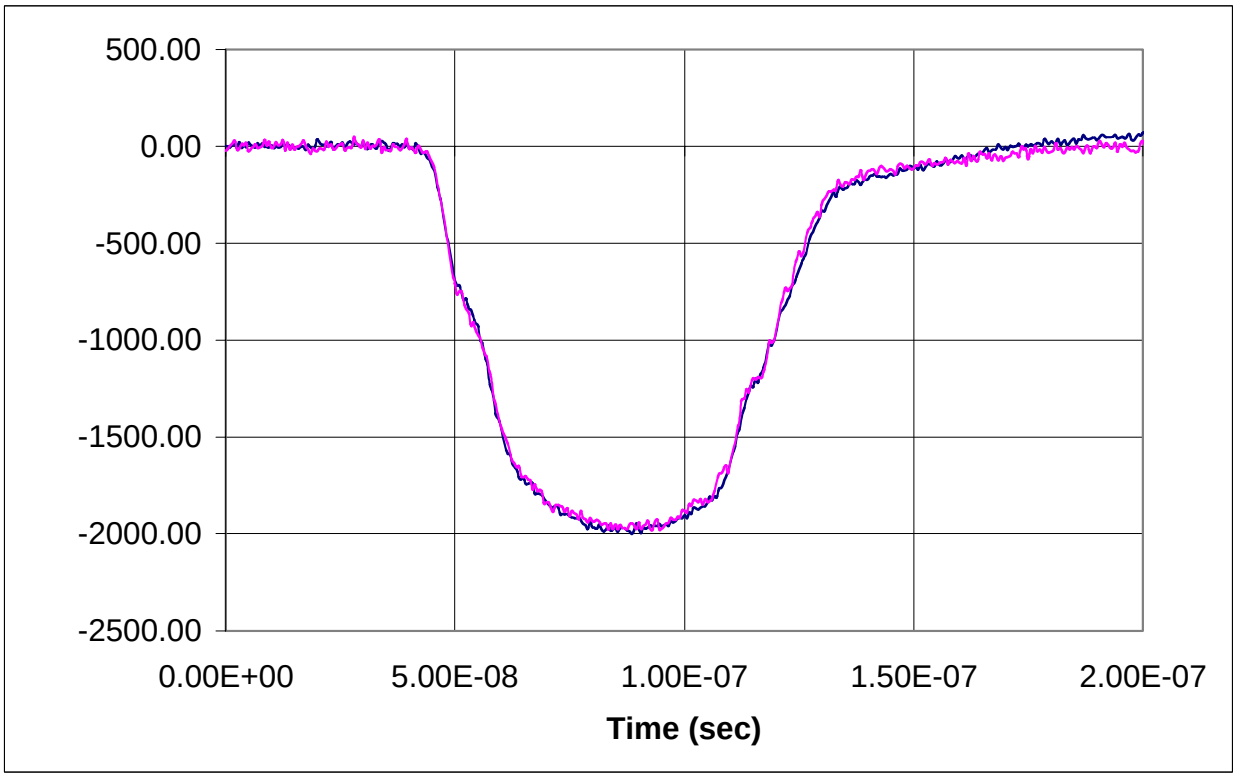

Figure 13 Overlay of DML and BBT05 current for EF0=5.5A.

decreases about 11 A between the DML and BBT05. If we further increase the BBT05 calibration to the point where this difference disappears, the eyeball fit is not as good. This is probably the limit on our measurement accuracy but the current difference between the two beam

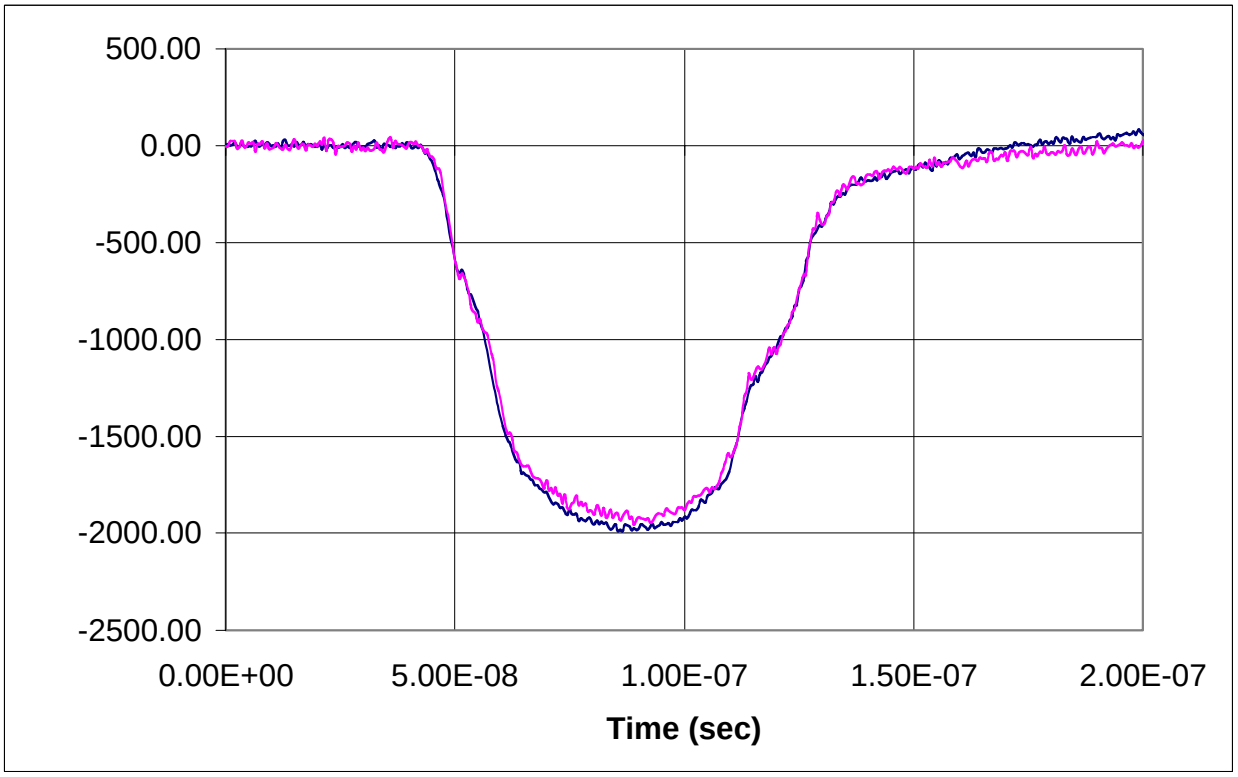

Figure 14 Overlay of DML and BBT05 current for EF0=4.5A.

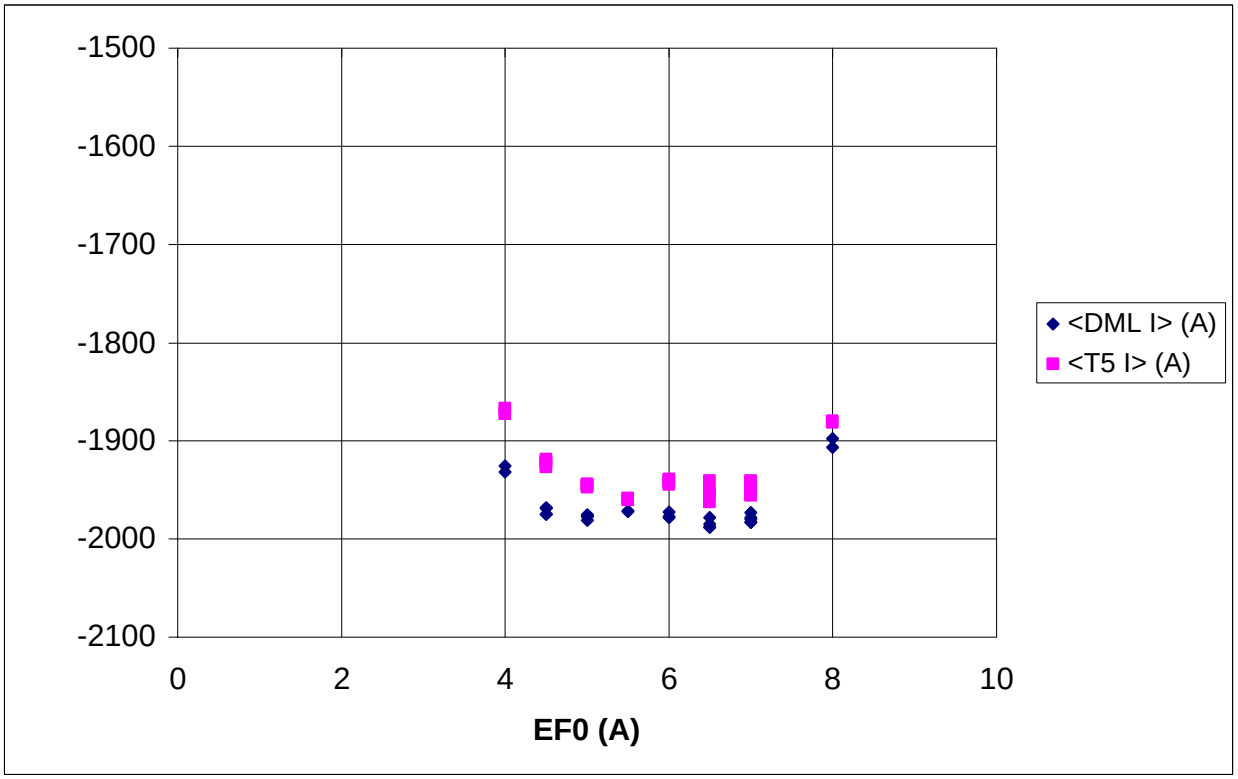

Figure 15 Peak beam current at the two beam bugs.

bugs is quite a bit larger than this for other settings of EF0. One such case is shown in Figure 14 where with the same calibration as for Figure 13 we now see a loss of over 50 A between the two beam bugs. In Figure 15 we plot the 10 ns average around peak current at the two beam bugs as a function of the EF0 setting for the full DML-foil data set. This shows that there is some current loss between the two beam bugs over the whole range of settings and at the extreme EF0 settings there is additional loss upstream of the DML.

For the distribution of Equation 24 the current density for $r < r_0$ is

$$j_{z0} = \frac{I}{\pi(r_0^2 + 2r_0\delta(R - r_0)} \qquad 0 < r < r_0 \qquad (27)$$

while at the wall the current density is

$$j_z(R) = \delta(r_0/R)j_{z0}\,. \qquad (28)$$

The average current density lost to the wall between the two beam bugs is

$$j_r(R) = \frac{\Delta I}{2\pi RL} \qquad (29)$$

where L is the axial separation of the two beam bugs (=22cm). For the model to be consistent with the observed losses it is necessary that the average angle of the beam particles hitting the wall to be

$$< r'(R) >= j_r(R)/j_z(R) = \frac{r_0(1-2\delta) + 2R\delta}{2L\delta}\frac{\Delta I}{I} \qquad (30)$$

In Figure 16 we plot the implied values of the average angle for the measured current loss and

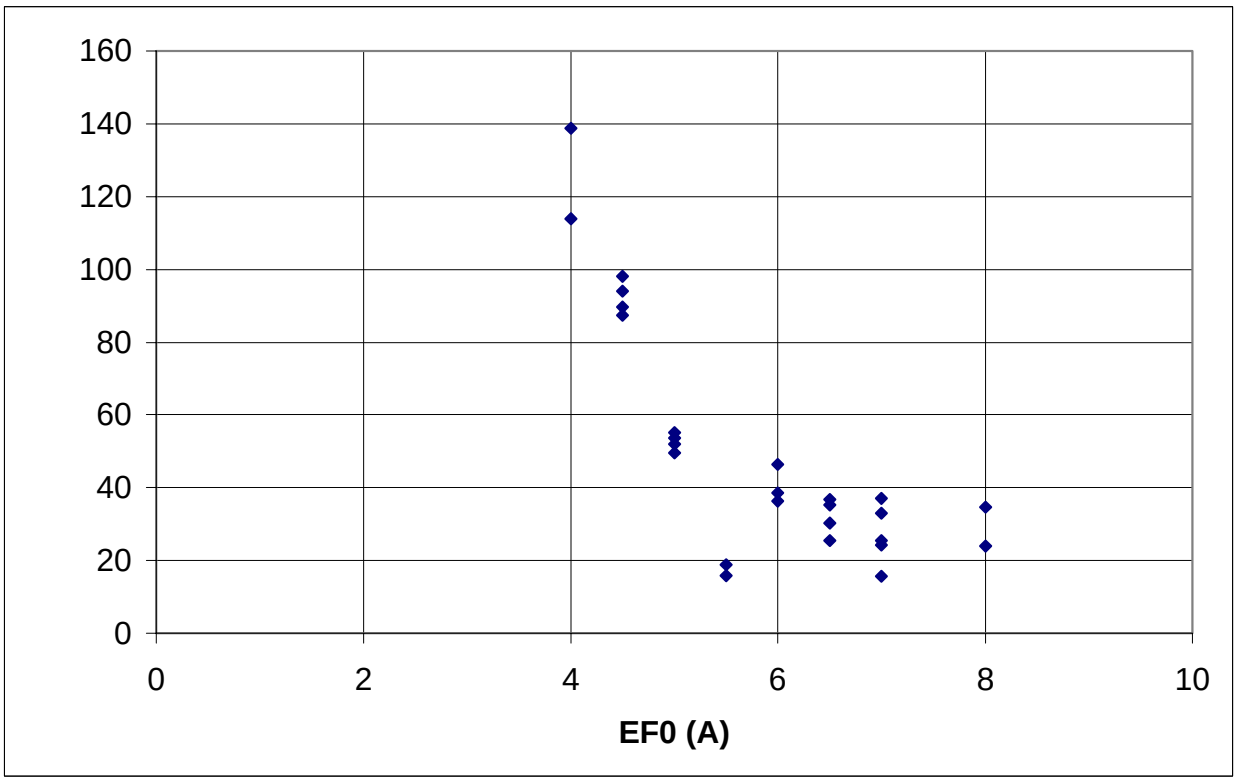

Figure 16 Average angle of particles hitting wall implied by current loss and halo model for del=0.022.

foil measurement of r_0, assuming $\delta = 0.022$. These values do not seem unreasonable; a straight-line path from the center of the DML to the wall at BBT05 makes an angle with the axis of about 300 mr.

I have presented a simple model of the radial beam current distribution and have shown that a rather low-density halo can explain the discrepancy between the two measurements. Signals due to wall bombardment and current loss to the walls are consistent with the model. Both DML and foil measurements may be necessary when working with beams with halos.

IV. DISCUSSION

We have demonstrated that DMLs can be used in a high current electron linac with an axially symmetric transport system to measure the magnetic moment of the beam. Under certain easily met conditions the time resolved beam rms radius can be derived from the moment measurements. This approach has the advantage over the present standard foil measurement of beam radius in that it is a non-interfering electrical measurement with good time resolution. The DML measures the total beam moment and thus the rms radius of the entire beam whereas the foil preferentially measures the parameters of the beam core. This is an important distinction if there is an appreciable beam halo.

In measuring the beam moment we are measuring the beam mechanical angular momentum. We have shown that this angular momentum can increase during the beams passage through the beam transport system, a violation of the conservation of canonical angular momentum that must be due to symmetry breaking by field errors or spotty cathode emission. Nevertheless we are still able to determine the beam radius at a DML by steering the beam close to the axis at the DML, adjusting the cathode field to minimize the DML signal in zero magnetic field, and, finally measuring the moment when the field at the DML is brought on to a known value. Thus it is possible to use this diagnostic in real accelerators that are never completely axially symmetric.

In principle, a three DML array could be used to yield a single shot time resolved reconstruction of the beam parameters, radius, slope of the beam envelope and emittance, at the array entrance. This would require that the beam is emittance dominated, that there is minimal current loss between the elements of the array, that the same setting of cathode field minimize the zero field signals of all three DMLs, i.e., that there is no momentum growth occurring between the elements of the array, and the energy be known and constant through the array. This appears possible with an array located in the drift region at the exit of the accelerator and in fact such an array is installed in FXR but time and funding have precluded its operation. The array concept is discussed in Appendix E.

ACKNOWLEDGMENTS

I wish to acknowledge the many who over the years have lent their support both physically and programmatically to this work. DML development grew out of discussions with George Caporaso and early work on ETA-II was encouraged and supported by Bill Turner. The work on FXR was supported in turn by Ray Scarpetti, and Jan Zentler while the later work on ETA-II by John Weir. On FXR I thank Mike Chaplin and Aaron Jones for software support and on ETA-II, Brett Raymond. I wish to thank Cliff Holmes for his careful work in building and modifying

almost all of the prototype and existing DMLs and Art Paul for many interesting and informative discussions. Finally I want to thank the FXR and ETA-II operating crews who were always willing to give a hand.

1. S. Drell,R . Jeanloz, and B. Peurifoy, "Arms Control: Maintaining a Nuclear Deterrent Under the Test Ban Treaty", Science, **283** 1119 (1999).
2. Y.-J. Chen et al., "Degradation of Brightness by Resonant Particle Effects", Proceedings of Fourteenth Particle Accelerator Conference (San Francisco,Ca, May 6-9,1991)
3. Yu. I. Abrashitov, V. S. Koidan, V. V. Konyukov, et al., Zh. Eksp. Teor. Fiz. **66**, 1324 (1974) [Sov. Phys. JETP **39**, 647 (1974)].
4. V. I. Erofeev, B. A. Knyazev, S. V. Lebedev, and V.V. Chikunov, Zh. Tekh. Fiz. **59**, 111-120 (1989) [Sov. Phys. Tech. Phys. **34**, 11561161 (1989)].
5. R. J. Adler, G. F. Kiuttu, and T. P. Hughes, Phys. Fluids **28**, 434-437 (1985).
6. W. E. Nexsen, "A Non-Interfering Beam Radius Diagnostic", UCRL-JC-108211 (1991).
7. D. Moir, private communication.
8. B.E. Carlsten, "Using the induced axial magnetic field to measure the root mean square beam size and beam density uniformity of an electron beam in an induction accelerator", Rev. Sci. Instrum.,**70**, 3308-3313 (1999).
9. C. Ekdahl, "Noninvasive measurement of electron-beam size with diamagnetic loops", Rev. Sci. Instrum.,**72**, 2909-2914 (2001).
10. T. J. T. Kwan, B. G. DeVolder, J. C. Goldstein and C. M. Snell, "Study of a Non-Intrusive Electron Beam Radius Diagnostic", Proceedings of the 1997 Particle Accelerator Conference, 2174-2176 (Vancouver, B.C.).
11. W. E. Nexsen,"Characterization of Field Errors of Layer Wound Short Solenoids", Proceedings of 1990 Linac Conference (Albuquerque, New Mexico,September 10-14, 1990).
12. K.W. Struve, "Electrical Measurement Techniques for Pulsed High Current Electron Beams", Proceedings of Conference on Measurement of Electrical Quantities in Pulse Power Systems-II,(National Bureau of Standards, Gaithersburg, Maryland, March 5-7, 1986).

APPENDIX A –FUNDAMENTAL MOMENT EQUATION

If a relativistic charged particle is directed along the z axis with velocity v, the field seen by an observer in the z=0 plane of the fixed system at a radius b due to this point charge q passing through the plane at t=0 is

$$B_\theta = \frac{\mu_0}{2\pi}\frac{\gamma v q b}{(b^2+\gamma^2 v^2 t^2)^{3/2}} \tag{A-1}$$

The time interval over which the field is appreciable is $\Delta t \approx \frac{b}{\gamma v}$ and the length of beam whose particles contribute to the observed field is $\Delta l \approx \frac{b}{\gamma}$. A segment of the particle beam of length Δl centered axially at z= 0 will create a field at the observer,

$$B_\theta \approx \frac{\mu_0}{2\pi}\frac{\gamma b I \Delta l}{b^3} \approx \frac{\mu_0}{2\pi}\frac{I}{b}. \tag{A-2}$$

As long as changes in the beam occur over distance long compared with Δl and in times long compared with Δt the field seen by the observer will be the same as that of an infinitely long beam of current I. For the FXR beam at the injector energy ($\gamma \approx 6$) and b=7cm, $\Delta l \approx 1.2$ cm and $\Delta t \approx 40$ ps.

An isolated circular loop located in a plane, z=constant, and centered on the axis will not link any flux under the above circumstances. If, however, the beam particle makes a small angle with respect to the axis there will be a z component of its field in the positive direction over one-half of the z plane and negative in the other. Using the theory of infinitesimal rotation [A-1] we find for $\frac{v_x}{v_z}, \frac{v_y}{v_z} << 1$

$$\begin{aligned} B_z &= B_x \Delta\Omega_y - B_y \Delta\Omega_x \\ B_z &= B_x \frac{v_x}{v_z} - B_y \frac{v_y}{v_z} \\ &= -\left(\frac{\mu_0 q v_z}{2\pi r}\right)\left[\sin(\varphi)\frac{v_x}{v_z} + \cos(\varphi)\frac{v_y}{v_z}\right] \end{aligned} \tag{A-3}$$

in the case where the particle passes through the origin in the plane of measurement. Because of symmetry a circular loop centered on the axis will have no net flux linking it.

If the particle is off axis a distance r as it passes through the plane of measurement the situation changes. We lose no generality by assuming the displacement lies along the x-axis. With this choice of coordinates, $v_y = v_\theta$ and $v_x = v_r$. Measuring r' from the particle intercept of the plane of the loop, the distance to the loop of radius b >>□ is $r' \cong b - r\cos(\varphi)$. The net flux linking the loop is

$$\begin{aligned} \delta\Phi &= \int_0^{2\pi}\int_0^{b-r\cos(\varphi)} B_z \, r' dr' d\varphi \\ &= -\left(\frac{\mu_0 q v}{2\pi}\right)\int_0^{2\pi}\int_0^{b-r\cos(\varphi)}\left[\sin(\varphi)\frac{v_r}{v_z} + \cos(\varphi)\frac{v_\theta}{v_z}\right] dr' d\varphi \\ &= \mu_0 q v_z \left(\frac{r v_\theta}{2v}\right) = \mu_0\left(\frac{r\delta}{2}\right)\delta I \end{aligned} \tag{A-4}$$

Equation A-4 is the fundamental moment equation from which Equation 7 of the main section follows

If $\frac{v_\theta}{v} \approx \frac{I_\theta}{I}$, i.e., if the variation in angle of the beam particles is small compared with respect to the theta component of their average value

$$\Phi = \mu_0(\frac{\rho I_\theta}{2I})I = \mu_0(\frac{\rho\delta}{2})I \qquad \text{(A-5)}$$

Here $\rho = \sqrt{x^2 + y^2}$ where x, y are the coordinates of the centroid intercept of the loop plane and δ, is the (small) angle between the plane defined by ρ and the axis and the plane defined by ρ and the beam centroid..

A-1. Goldstein, Herbert, *Classical Mechanics.* Cambridge: Addison-Wesley Press, 1950 (Chapter 4).

APPENDIX B-LOOP CALIBRATION

A. Apparatus

For the bench top calibration of the DML we sandwich the beam bug between two lengths of stainless steel tubing that simulate the flux conserving beam tube and measure the loop's response to a small diameter pulsed solenoid, inserted along the loop axis. This calibration coil is fashioned from a 0.5 m length of RG 65 A/U video delay cable. The inner conductor of this cable is a 3.25 mm diameter solenoid with ~4.2 turns/mm of No. 32 Formex insulated wire. We replaced the flux conserving outer shield with eight equally spaced, axis-parallel, straight insulated wires carrying the return current and the whole was encased in a close fitting Lucite tube to give it stiffness. The far end is terminated with eight parallel 10 K ohm carbon resistors giving a measured termination resistance of 1276 ohm. This value, which minimized the pulse reflection coefficient, is markedly different from the 950 ohm impedance of the standard shielded cable. The coil is fed through an impedance matching network by a 100 ns pulse from a spark gap switched 50 ohm line. In most cases the signals from the two DML terminals are fed to a hybrid coupler and their difference $V=V_B-V_A$ (for $\theta_B>\theta_A$ in the accelerator coordinate system) recorded at half nanosecond intervals on one channel of a four-channel Tektronix 644A digital scope while the voltage drop across a 1.4 ohm resistance in series with the coil (hereafter referred to as the coil current signal) is recorded on a second channel. The system is presently limited to a 200 MHz bandwidth by the hybrid coupler so the data is recorded with a 100 MHz scope bandwidth setting. The signal from a ~15 mm diameter single turn loop, closely wound on the calibration

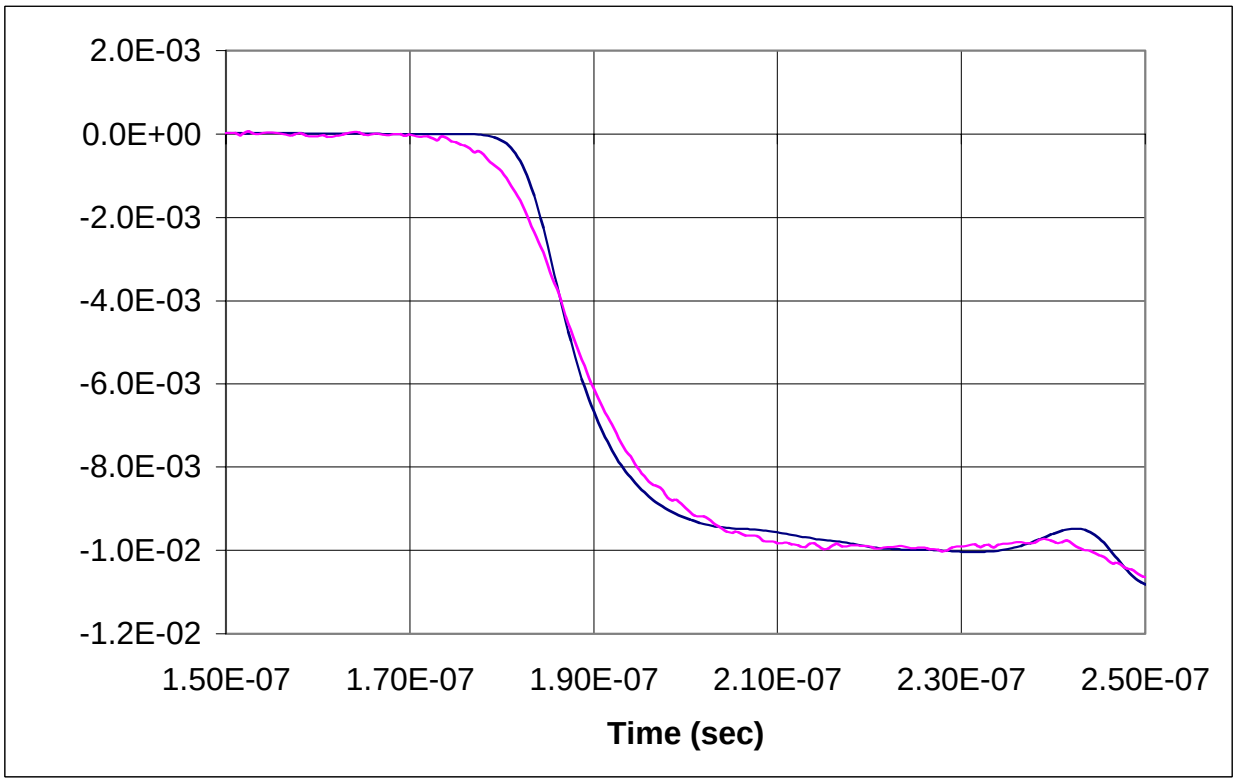

Figure B-1 Overlay of coil moment from reduction of DML and small loop data.

coil in the plane of the DML is recorded at similar intervals on a third scope channel. The net flux linking this loop is the difference between that due to the calibration coil and the return flux forced through the loop by the flux conserving walls and is ~99% of the calibration flux. From this it follows that the small loop integrated signal when divided by $0.99\mu_0$ gives the magnitude and time variation of the calibration coil magnetic moment in the DML plane.

B. Procedure

The calibration procedure has gone through several iterations before arriving at the present approach. Initially it was thought that knowledge of the calibration coil geometry and measurement of coil current signal would be sufficient for the loop calibration. This ignored two problems: first, the calibration wave front propagates along the coil at a velocity of 0.81 cm/ns, consequently a fast rising coil signal produces a much slower rising loop signal as the calibration wave passes through the loops sensitive region and, secondly, the calibration wave is heavily attenuated as it travels down the coil. The realization of the importance of these effects led to the use of the small loop to measure the moment directly, which in turn led to some further complications. The small pickup loop and the DML are sensitive to flux changes over coil lengths of the order of their respective radii. Because of the disparity in their radii we would not expect them to have exactly the same time response when the calibration wave passes through them. This is illustrated in Figure B-1. We use a Gaussian weighted running average of the small loop signal with an e-folding time of 6.6 ns to simulate moment variation over the region of sensitivity of the larger loop (Figure B-2).

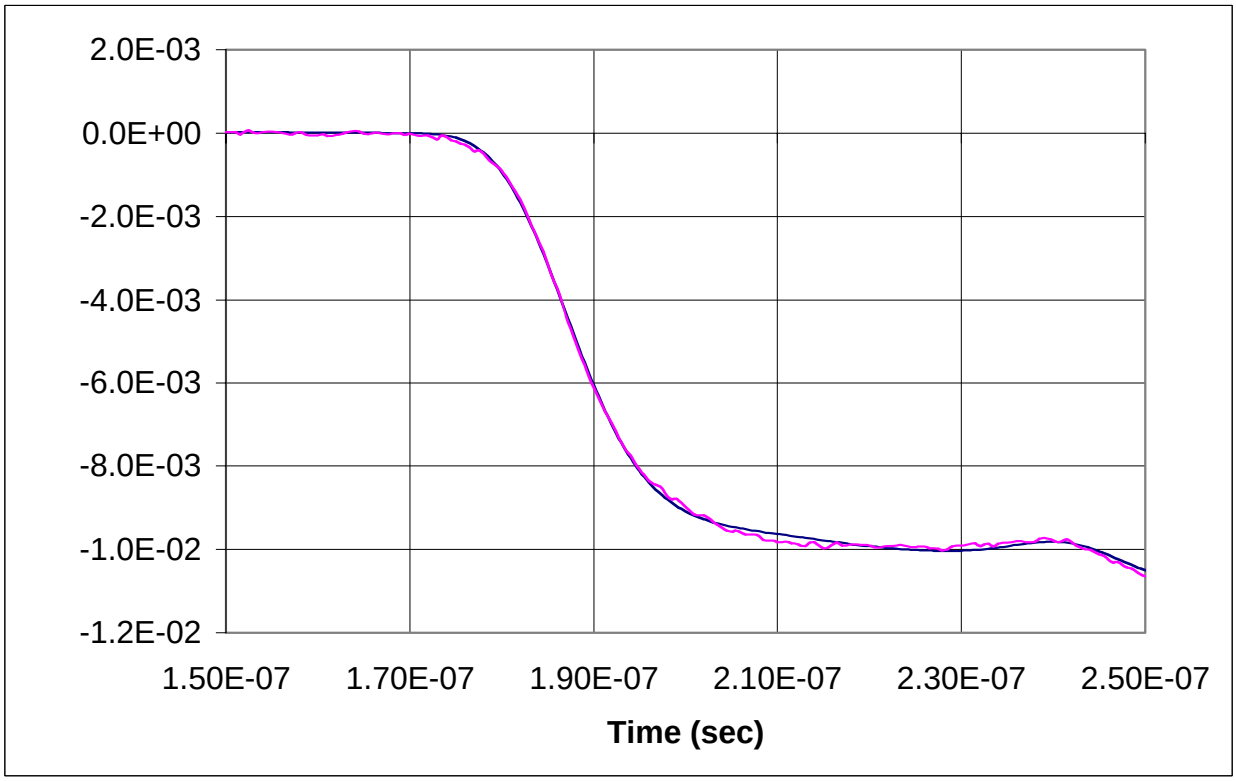

Figure B-2 Same data but with Gaussian weighted running average of small loop data with e-folding time of 6.6 ns.

Figure B-3 shows a typical small loop raw signal. Because of the wide dynamic range of the signal, there is appreciable bit noise which when integrated introduces a random walk component

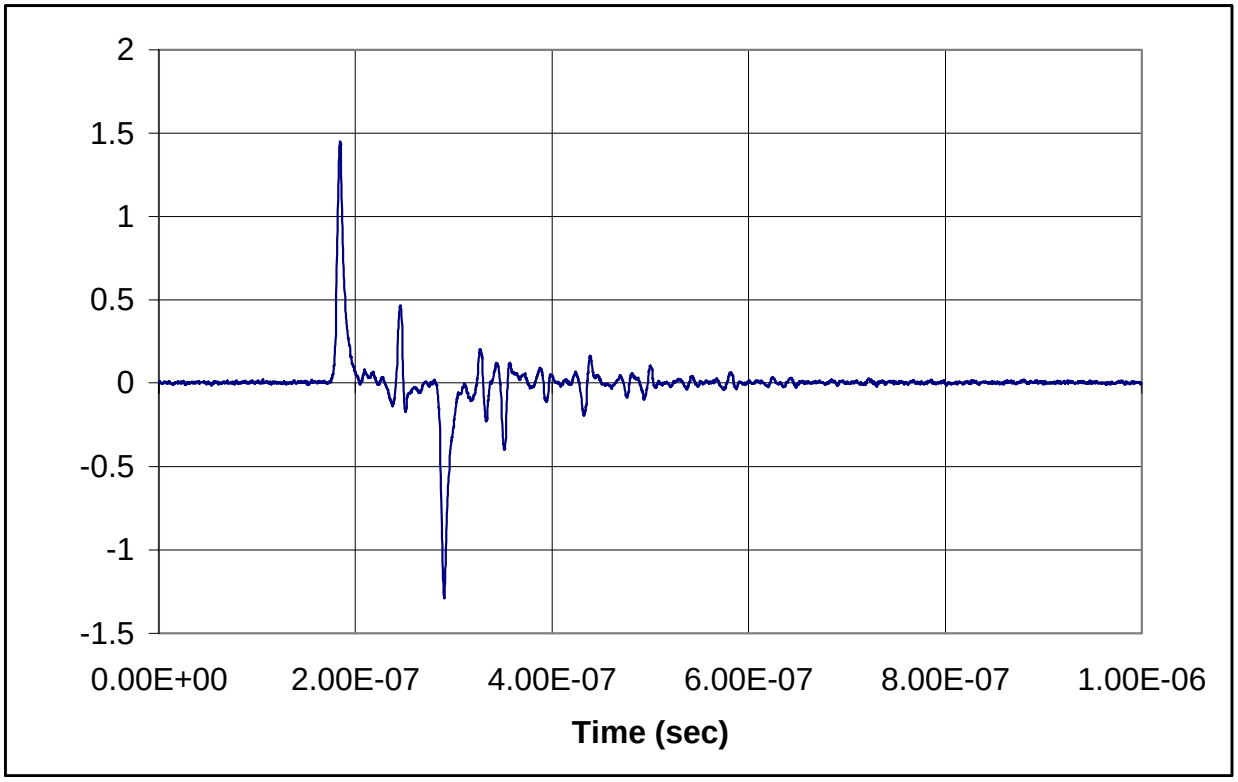

Figure B-3 Typical small loop raw signal.

with the result that the integrated signal usually does not return to zero late in time. To minimize this problem we use a master normalized moment signal. Eighty small loop data records were baseline subtracted, integrated, averaged, and the result Gaussian spread. This data was normalized to the calibration coil signal, averaged over a period of fifty nanoseconds after the first peak, and forced to zero late in time by subtracting a ramp beginning at the start of the signal. Figure B-4 shows that this subtraction had little effect on the integrated signal.

The overlay of Figure B-2 shows evidence of overshoot by the DML signal. We have observed this in a number of cases and conjecture that it is caused by the parasitic capacity of loop twisted pair leads and/or the hybrid junction. To compensate for this effect we have added some terms to the DML data reduction algorithm ***A***,

$$\boldsymbol{A}(\tau_1,\tau_2,\omega) \equiv \frac{\tau_2}{\omega^2}\frac{d^2V(t)}{dt^2} + (\tau_1\tau_2 + \frac{1}{\omega^2})\frac{dV(t)}{dt} + (\tau_1+\tau_2)V(t) + \int_{-\infty}^{t} V(t')dt' \qquad \text{(B-1)}$$

Here, V(t) is the baseline subtracted raw DML signal and τ_1, τ_2, and $1/\omega^2$ are fitting parameters which can be identified with the loop and foil L/R times respectively and the LC of the loop inductance and parasitic capacity. When τ_1, τ_2, and $1/\omega^2$ have their proper values the net flux linking the loop, numerically equal to the flux returning external to the loop, is $\Phi(t) = \frac{1}{N}\boldsymbol{A}(\tau_1,\tau_2,\omega)$.

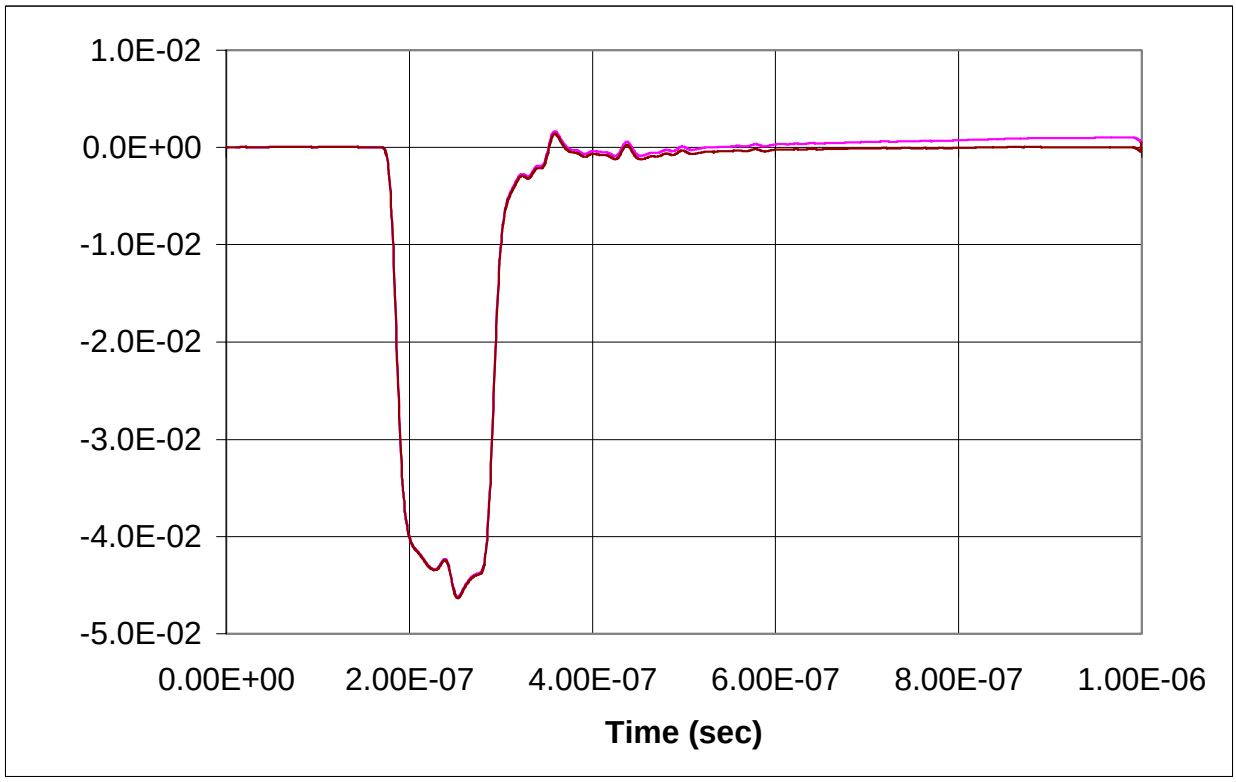

Figure B-4. Overlay of master normalized moment, with and without ramp subtraction.

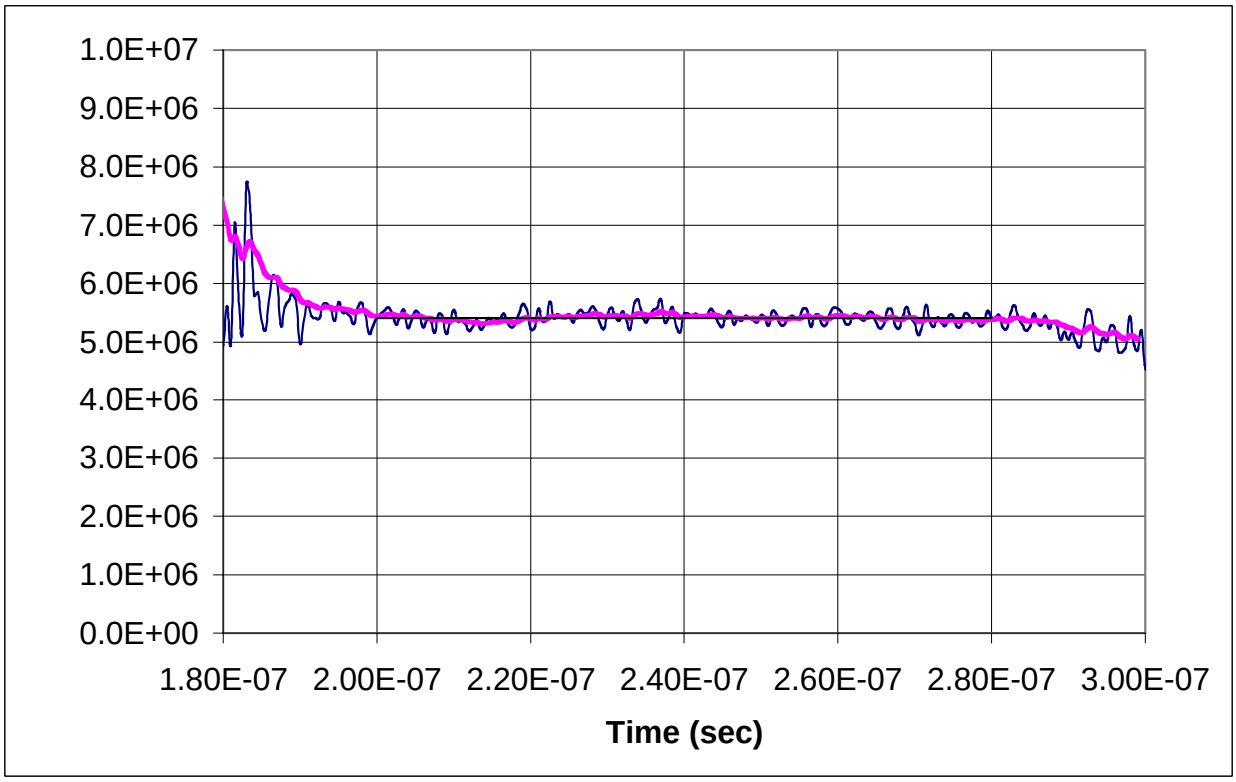

Figure B-5. k(t) for optimized set of parameters.

During the loop calibration we use Equation (14) to generate

$$k(t) = \frac{(M(t)/V_c)_{cal} V_c}{\boldsymbol{A}(\tau_1, \tau_2, \omega)} \qquad \text{(B-2)}$$

Here V_c is the average coil current signal value. Ideally, when τ_1, τ_2, and ω have their correct values, the denominator of Equation (19) should track $M_{cal}(t)$ and k(t) should be constant. We use a spreadsheet to generate k(t) and the function ***S***

$$\boldsymbol{S} \equiv 1 - \frac{\text{Standard deviation of mean of k(t)}}{\text{Average k(t)}} \qquad \text{(B-3)}$$

during a period of 80 ns beginning 25 ns after the moment first begins to rise. Maximizing ***S*** will minimize any long term trend in k(t). We maximize this function by a search in a multidimensional parameter space composed of τ_1,τ□,ω and the time shift between the two signals. Figure B-5 shows k(t) from Equation B-2 for an optimized set of parameters before and after smoothing. The smoothing minimizes the high frequency variation due to noise and allows one to pick up slower trends. Figure B-6 is an overlay of the calibration moment and the output

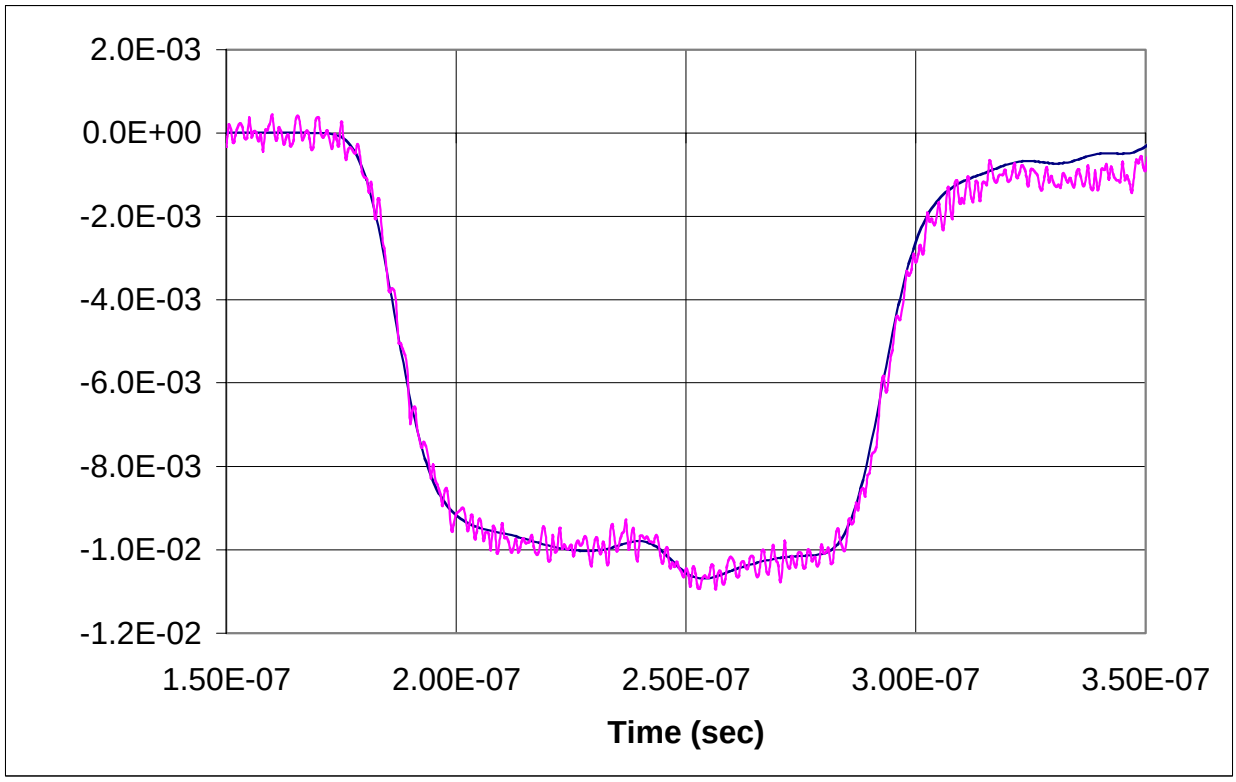

Figure B-6. Overlay of reduced DML signal and calibration moment for data of Figure B-5.

of Equation 14 for the data and parameters of Figure B-5. For this case, <k(t)>= 5.46E+06 ± 4.2E+04 A-m/V-sec, τ_1= 8.4 ns, τ_2= 34.6 ns, ω= 7.5E+08 and ***S***= 0.99940. You may notice that the fit is not good late in time. This appears to be a result of flux having soaked into the resistive beam tube wall and is discussed in Appendix C.

C. Discussion

Seven FXR and one ETA-II beam bugs have been modified with balanced loops and calibrated. The first built has a single turn loop while the later ones have two turns. Of these six are now mounted on FXR. Three of these were calibrated using a 300 ns pulse and one of these, the original one, was not calibrated with the small loop. Fortunately all of the calibration data has included simultaneous recordings of the coil current signal, so we have been able to use the process described above to re-reduce the old data while concentrating on the first 100 ns of the pulse. We estimate with this approach $\langle k(t) \rangle$ has a standard deviation of the order of ±2%.

Several comments are in order concerning the calibrations. It was noticed that the calibration results varied somewhat if a different hybrid was substituted; consequently the loop should be calibrated with the hybrid to be used in the measurement. The hybrid was found to reduce the loop signal to approximately 0.6 of that without. In going from a one-turn to a two-turn loop the sensitivity more than doubled. This is believed to be the result of deepening the groove in the rexolite cylinder of the two turn loops, thus reducing the mean diameter of the loop and allowing more flux to return external to the loop. We also note that the loop time constant did not quadruple with the doubling of the number of turns, probably because the deeper groove decreased the gap between the wires and the foil, thus reducing the inductance.

We find that the ETA-II DML is over twice as sensitive as the FXR DML. It is slightly smaller in radius (6.7 cm versus 7.3 cm) but more importantly the cavity behind the foil is wider, allowing more flux to return external to the loop. We can estimate the fraction of the primary flux that returns external to the loop from the relation $f = 1/kN\mu_0$. Here k is the experimental DML calibration constant (without hybrid), N is the number of turns in the loop and μ_0 is the free space permeability. For the ETA-II DML, N=2, k=1.580E+06, we find f is of the order of 25%, very close to the ratio of the area external to the loop to the total area which is about 30%.

No attempt has been made at a bench top DML calibration for the case of a skewed beam but we argue that a calibration constant of the same order as the above should apply. Equation A-5 of Appendix A applies for an isolated loop but must be modified for the case when there is a beam tube because the I_θ component of the beam current induces a flux conserving azimuthal current in the wall. The loop signal is produced by the time varying flux, due both to the skew beam and the wall currents, linking it. As a consequence the loop response is little different from that to the other moment components. Using a second beam bug separated from that containing the DML by a drift region one can obtain the isolated skew moment but the component of the loop response due to the this moment in the presence of the beam tube would only be about a quarter of this value (in the case of the ETA-II DML), i.e., the measured moment $M=M_r+M_\rho+M_u-M_c$ with $M_\rho \approx f \rho\delta I/2$.

APPENDIX C-LONG PULSE EFFECT

In Figure C-1 we plot a typical raw DML signal from a 300 ns calibration pulse while in Figure C-2 we plot the overlay of a long pulse calibration moment obtained from the reduction of the average of 28 small loop signals and the reduced data of Figure C-1. The DML detects a signal throughout the pulse that corresponds to a slowly changing flux, increasing during the pulse then slowly decaying later. The effect if present is nowhere as noticeable in the small loop

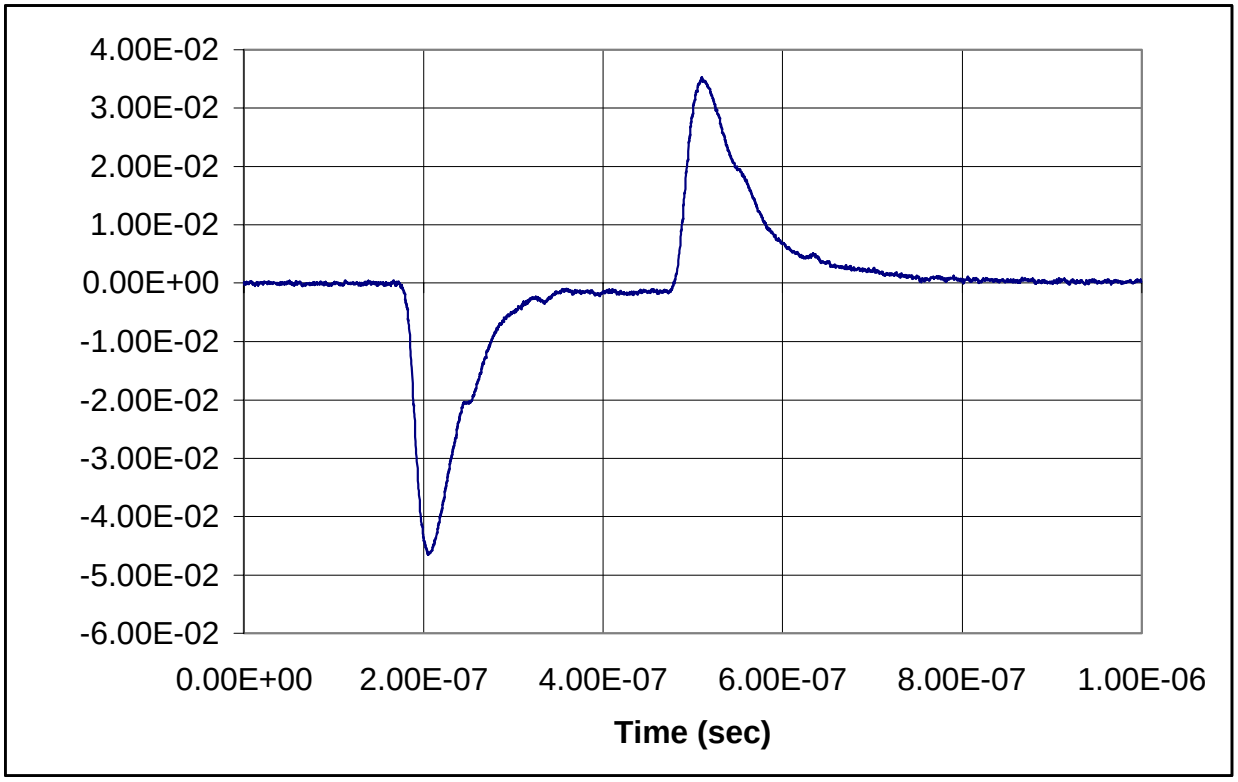

Figure C-1 Typical DML response to 300 ns calibration pulse.

data. Our survey of our database of calibration data confirms that this is a real phenomenon, not connected to the presence of the foil or ferrite. Shortening the pulse reduces the effect and is the chief reason we went from the 300 ns to the 100 ns calibration pulse that more nearly simulates the beam pulse length (Figure C-3). We hypothesize that the low level signal of Figure C-1 occurs because flux is soaking into the wall and as a consequence the net flux linking the loop is changing, even though the primary calibration moment may not be changing. We introduce a simple model to estimate this effect. For this model we assume that the loop of radius r_l is located within but close to and coaxial with the beam tube wall of radius r_{W0}. The wall is thick enough that no flux completely penetrates it during the time of the experiment. With flux conservation the fraction of the total flux linking the loop is

$$f = (1 - \frac{r_l^2}{r_w^2}), \qquad \text{(C-1)}$$

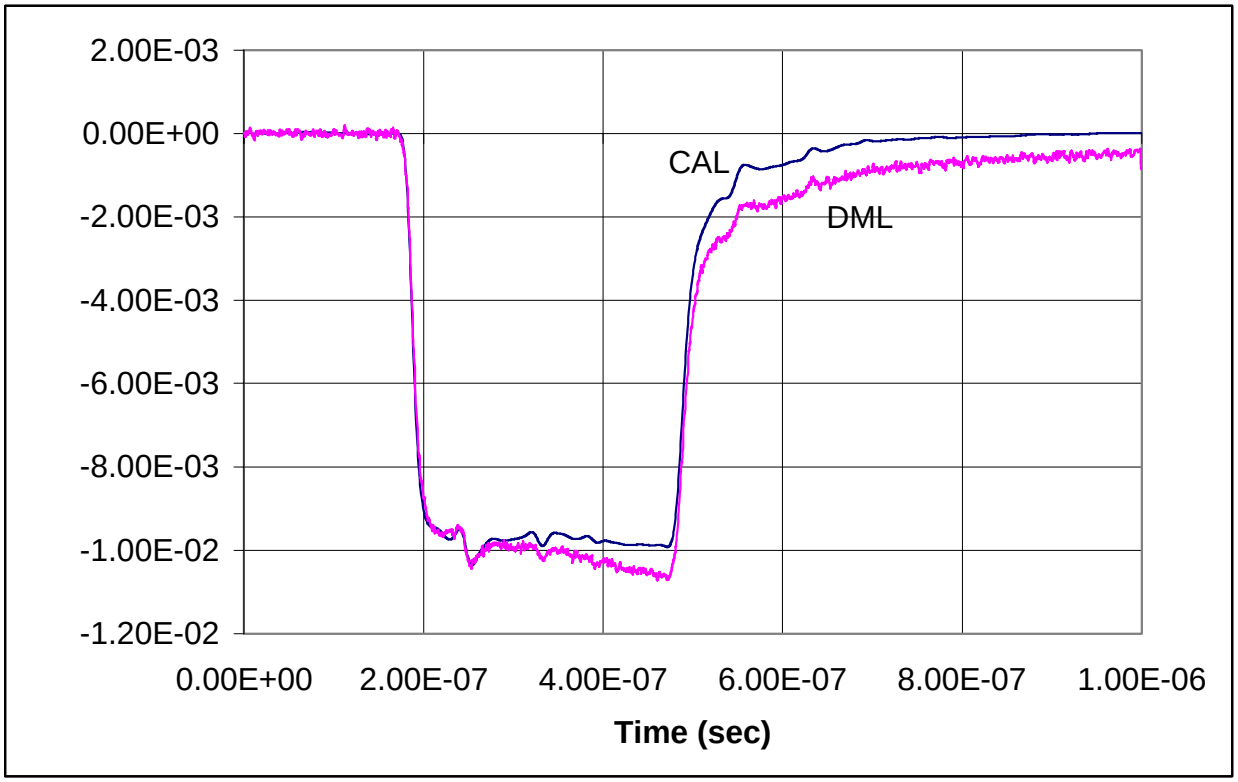

Figure C-2 Overlay of long pulse calibration moment and above data reduced.

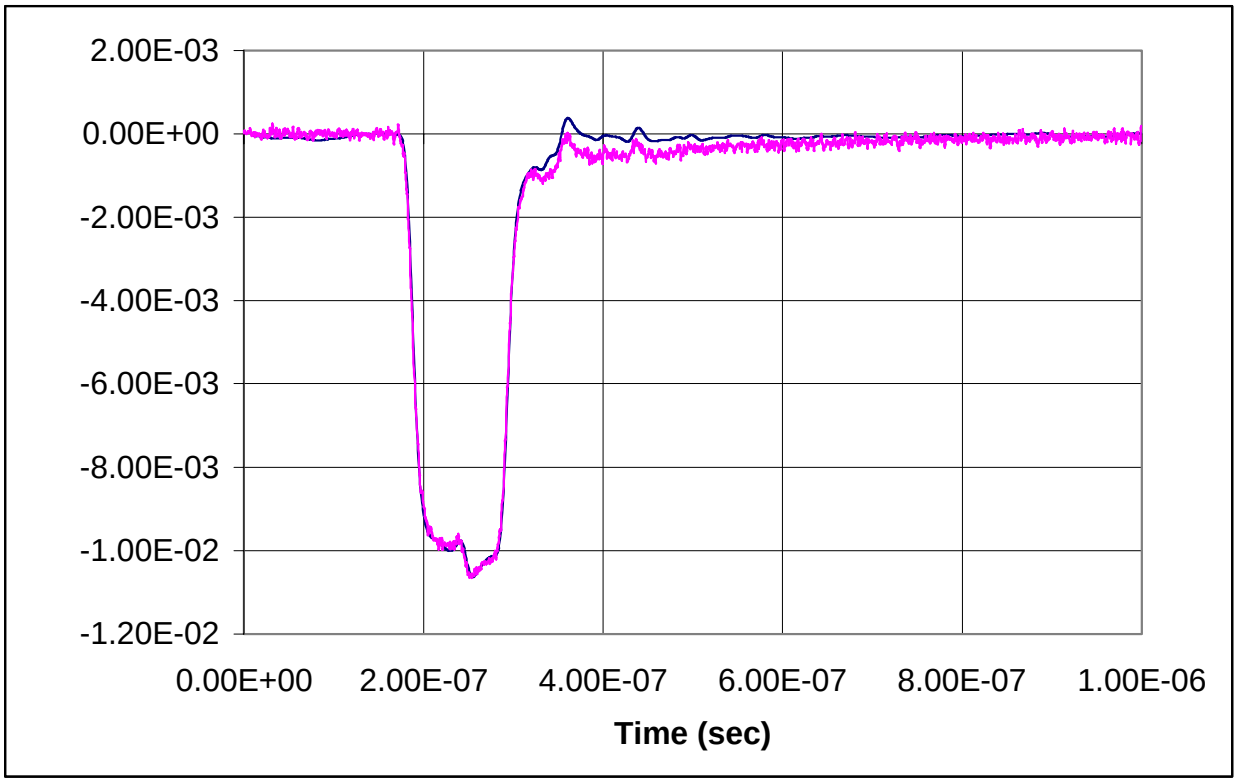

Figure C-3 Overlay of short pulse calibration moment and reduced DML data.

and the loop signal is

$$V = -N\frac{d(f\Phi_c)}{dt} = -N(f\frac{d\Phi_c}{dt} + \Phi_c\frac{df}{dt}), \qquad \text{(C-2)}$$

where Φ_c is the calibration coil flux and N is the number of turns in the loop. If, due to its finite resistance, flux is soaking into the wall

$$r_w(t) = r_{w0} + \delta(t)$$

$$r_w{}^2 \approx r_{w0}{}^2(1 + 2\frac{\delta}{r_{w0}}) \qquad \text{(C-3)}$$

$$f \approx 1 - \frac{r_l{}^2}{r_{w0}{}^2}(1 - 2\frac{\delta}{r_{w0}}) = f_0 + 2\frac{r_l{}^2}{r_{w0}{}^2}\frac{\delta}{r_{w0}}$$

for the case when $\delta(t) << r_{w0}$. For a step function calibration signal starting at t=0 the fractional change in the integrated loop signal with time will be

$$\frac{\Delta\int Vdt}{\int Vdt} \approx 2\frac{(1-f_0)}{f_0}\frac{\delta(t)}{r_{w0}}. \qquad \text{(C-4)}$$

Experimentally, we can estimate f_0 from the DML calibration constant. To avoid the attenuation introduced by the hybrid coupler the DML signal of Figures C-1, C-2 was recorded on two data channels and summed in software. We use the calibration constant for this data in

$$f_0 = \frac{1}{N\mu_0 k_{cal}} \quad . \qquad \text{(C-5)}$$

For N=2 and k_{cal}=3.5E+06, $f_0 \approx$ 0.1 (This is for an FXR DML, for ETA-II $f_0 \approx$0.25). We identify $\delta(t)$ as the skin depth , $\delta(t) = \sqrt{\frac{t}{\pi\mu\sigma}}$, and for a 0.073 m stainless steel beam tube, $\frac{\Delta\int Vdt}{\int Vdt} \approx 110\sqrt{t}$. For a 300 ns step function calibration pulse, we would expect the reduced DML signal to have risen by 6% by the end. In Figure C-2, the observed rise is about 7%.

At the end of the calibration pulse, an azimuthal current is induced in the beam tube wall opposite in direction to the original induced current. The flux soaked into the wall is trapped between the two layers that continue to diffuse radially as the energy of the trapped field is dissipated in the wall resistance. The flux must return inside the beam tube and a fraction, $(1-f_0)$, returns within the loop where it generates the long low-level signal late in time.

The signal perturbations due to the field soaking into the walls is of little importance for FXR because of its short current pulse but would be important in DARHT where with the FXR design DML, the reduced signal would have risen 15-20% by the end of a 2 μs step function calibration pulse. The present DARHT DML design is cantilevered within the beam tube wall, greatly increasing f to the point that the effect may not be important; however if it was found necessary to use the FXR design it could be improved by increasing the ferrite cavity width to increase f and using higher conductivity beam tube walls. In any case this design could be used after the beam is chopped.

APPENDIX D-DATA REDUCTION

In this section we discuss the requirements for an accurate beam radius measurement and present an example of the data reduction process. A valid measurement requires:

- Beam current and DML calibration
- Simultaneous recording of beam current, position, and DML signals.
- Beam centroid position at the loop << beam radius.
- Field at the cathode optimized.
- DML local field on and its value known.
- The value of γ at the DML.

In the following example a hybrid coupler was used to combine the two loop signals and the four signals, V_I, ΔV_X , ΔV_Y and DML hybrid difference, were recorded on a four channel digital scope(±1.5% accuracy) and read out after a shot into a spreadsheet where the data was reduced. The DML calibration has been covered in Appendix B. In the case of FXR, three of its beam bugs, none of which had modified DMLs, were calibrated on an airline before mounting on FXR. After determining that these three agreed both in magnitude and time variation in their measurement of beam current, they were used to cross calibrate the remainder of the FXR bugs using the beam current signal. The absolute calibration of the beam current measurement is believed to be good to better than ±3%. A special fixture was used to position a precision Hall-meter on axis in the plane of the DML to obtain B/I for the magnets contributing to the field at the DML. The beam energy, at present, is estimated from cell voltages and is believed to be our largest source of error, of the order of ±5%. The beam centroid position is calculated using the relation

$$x,y = \frac{R}{2}\frac{\Delta V_{x,y}}{V_I} \qquad \text{(D-1)}$$

Here R is the radius of the foil, $\Delta V_{x,y}$ are the x and y difference signals and V_I is the average current signal. Since the reduction requires the division of the three other signals by the current signal it is important that they be recorded as simultaneously as possible. To this end cable lengths are matched and signals shifted in the spreadsheet. We are limited in how close we can set this by the finite size of the time step (in the present case to <0.5 ns).

This shot data comes from a DML located in the drift region of FXR where $\gamma \approx 34$ and the loop field is 452G. It was taken after the optimization of the cathode field described in section III *A* of the main text and was recorded at 0.5 ns intervals. This time step is much smaller than necessary considering that the hybrid coupler has a bandwidth of 200 MHz and the scope bandwidth is set to 100 MHz but the redundancy allows one to do some smoothing of bit noise if necessary without further reducing the bandwidth. In this data set this property has not been exploited. In Figure D-1 we plot the raw voltage signals on an expanded time scale. From the figure we can see that the position signals do not begin to rise until 5 ns after the current and DML signal, indicating that their signal cables are too long. Before reduction these signals will be shifted 5ns earlier in time in the spreadsheet after which all are corrected for any baseline shift by subtracting the average signal before the arrival of the beam.

We use Equation (D-1) to reduce the position data and solve for the centroid radius $\rho = \sqrt{x^2 + y^2}$. This is plotted in Figure D-2 where we see that the centroid is within 1 mm of the

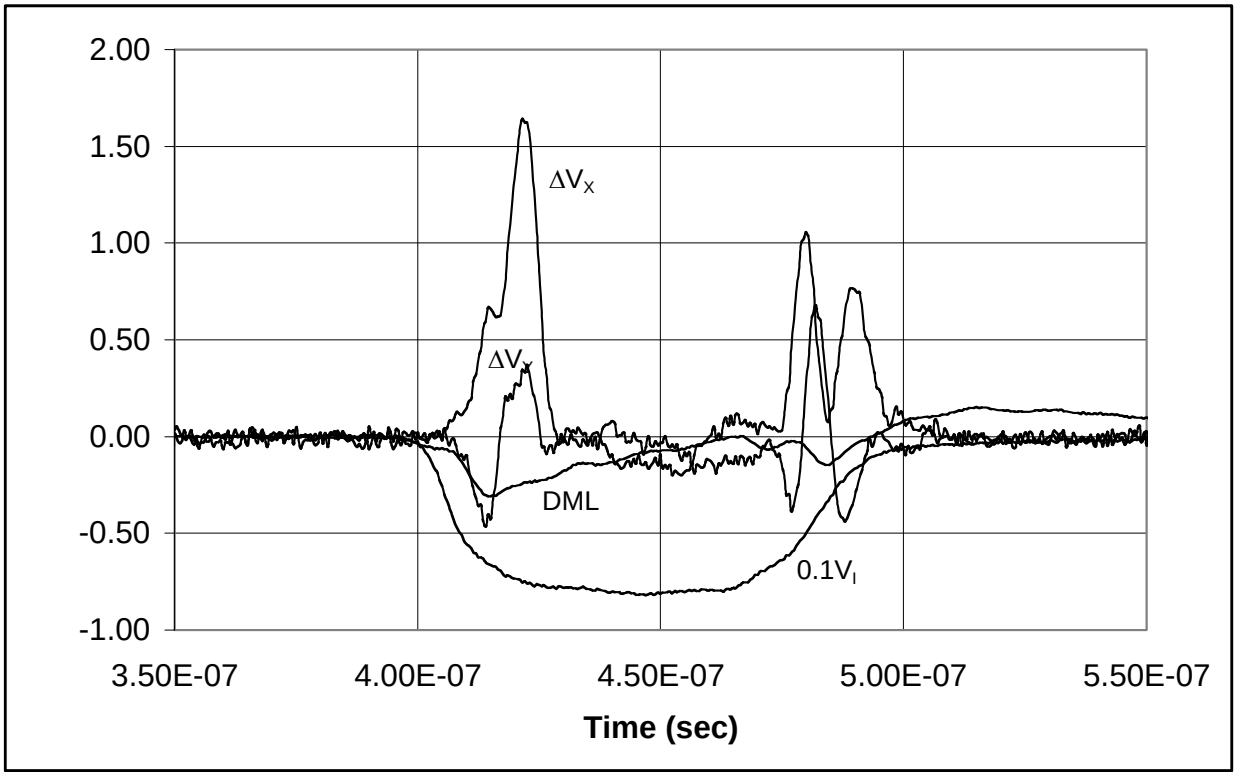

Figure D-1 Raw signals.

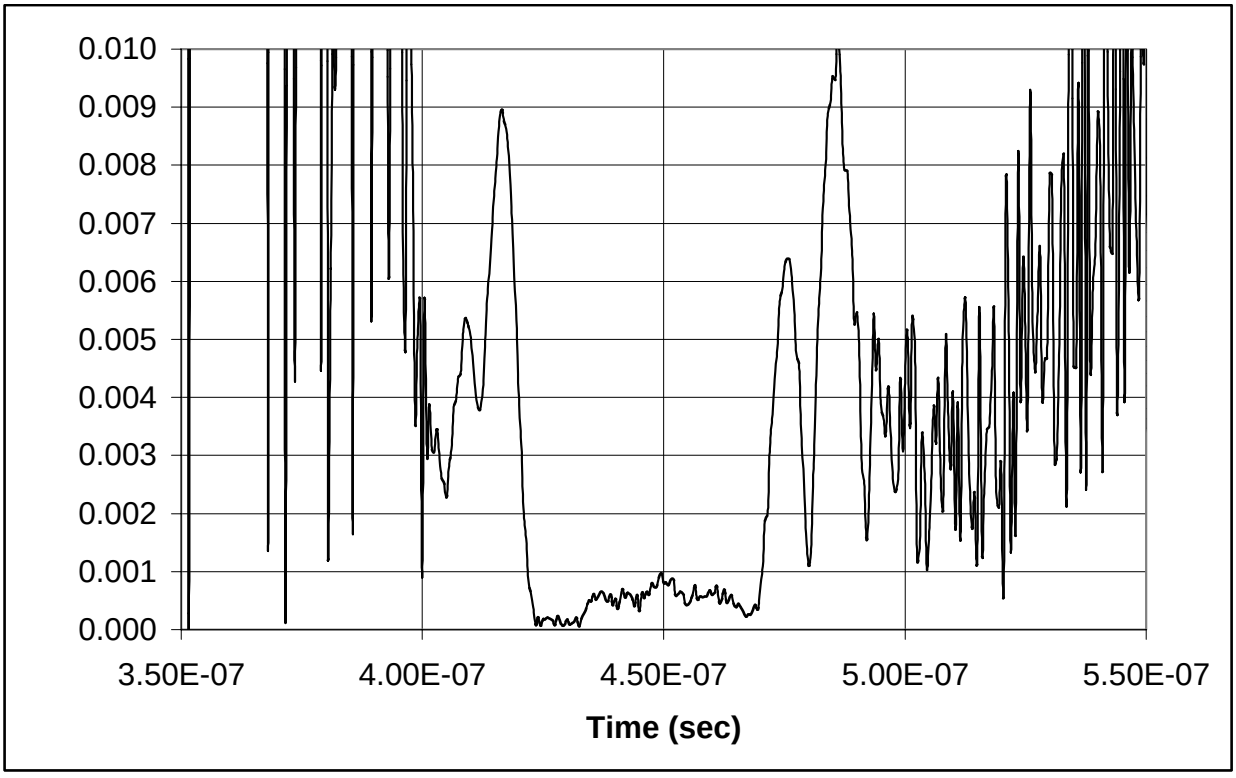

Figure D-2 Centroid radius.

axis for almost 50 ns. The large excursions of the centroid both before and after this period are probably evidence of energy variation advancing or retarding the phase of a spiraling beam.

If V(t) is the baseline subtracted raw DML signal, the beam magnetic moment is

$$M(t) = k[\frac{\tau_2}{\omega^2}\frac{d^2V(t)}{dt^2} + (\tau_1\tau_2 + \frac{1}{\omega^2})\frac{dV(t)}{dt} + (\tau_1 + \tau_2)V(t) + \int_{-\infty}^{t} V(t')dt'] \qquad (14)'$$

For this DML, hybrid combination, τ_1= 9.1 ns, τ_2= 37.4 ns, $\omega^2 \rightarrow\infty$, and k= 6.329E+06 (A-m).The important terms in the bracket of Equation (14)' are plotted in Figure D-3 while the resultant moment is shown in Figure D-4. Division of the moment by the current gives Figure D-5.

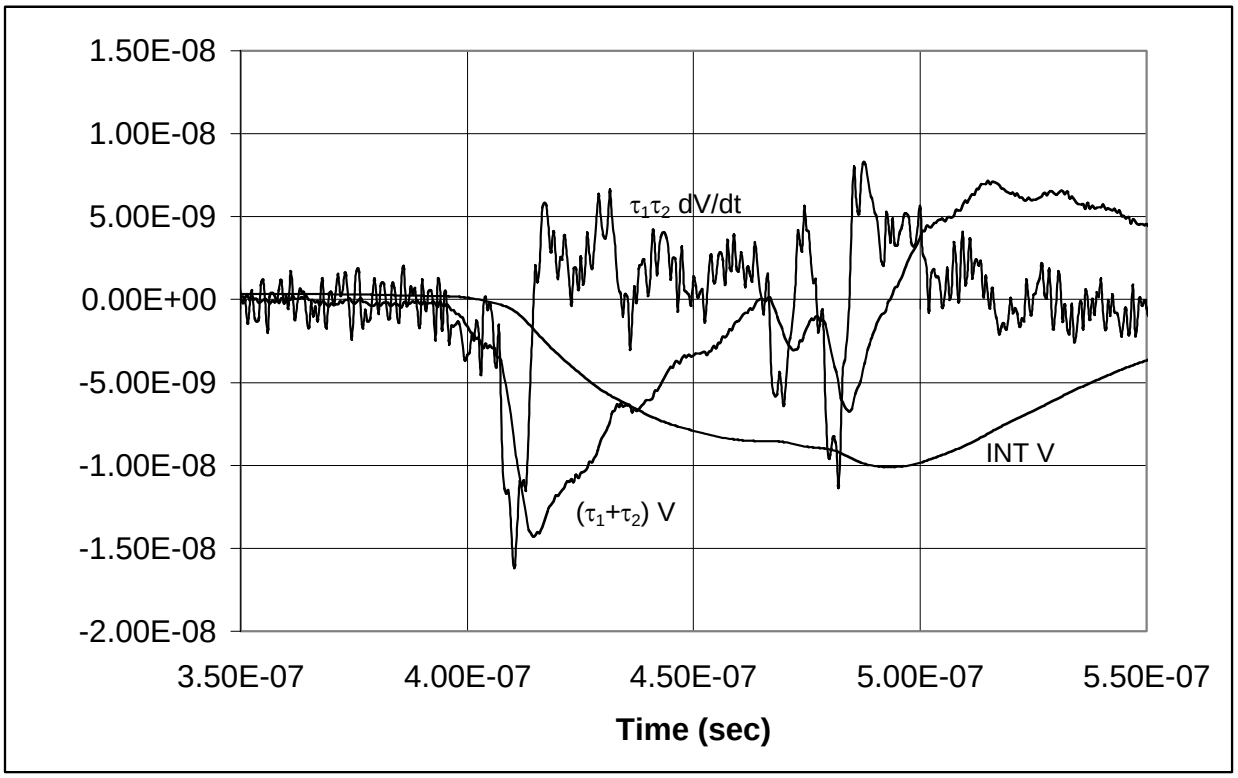

Figure D-3 Terms of Equation (14)'

Solving Equation (10) for the rms radius give $\underline{r} = \sqrt{\frac{4}{k_{ce}}\frac{M}{I}}$ where $\frac{4}{k_{ce}} = \frac{4\sqrt{\gamma^2-1}}{587B(T)}$ (m). The beam rms radius derived from the data of Figure D-5 for γ = 34 is plotted in Figure D-6. The radius is about a centimeter during the almost 50 ns period around the current peak. Outside of this time interval we can say little about the beam size, both because the energy is changing and because the beam centroid is undergoing large excursions from the axis. The addition of an energy analyzer measurement would allow us to correct our data for energy variation but, unless we can limit the size of the excursions, radius data during these periods will be suspect.

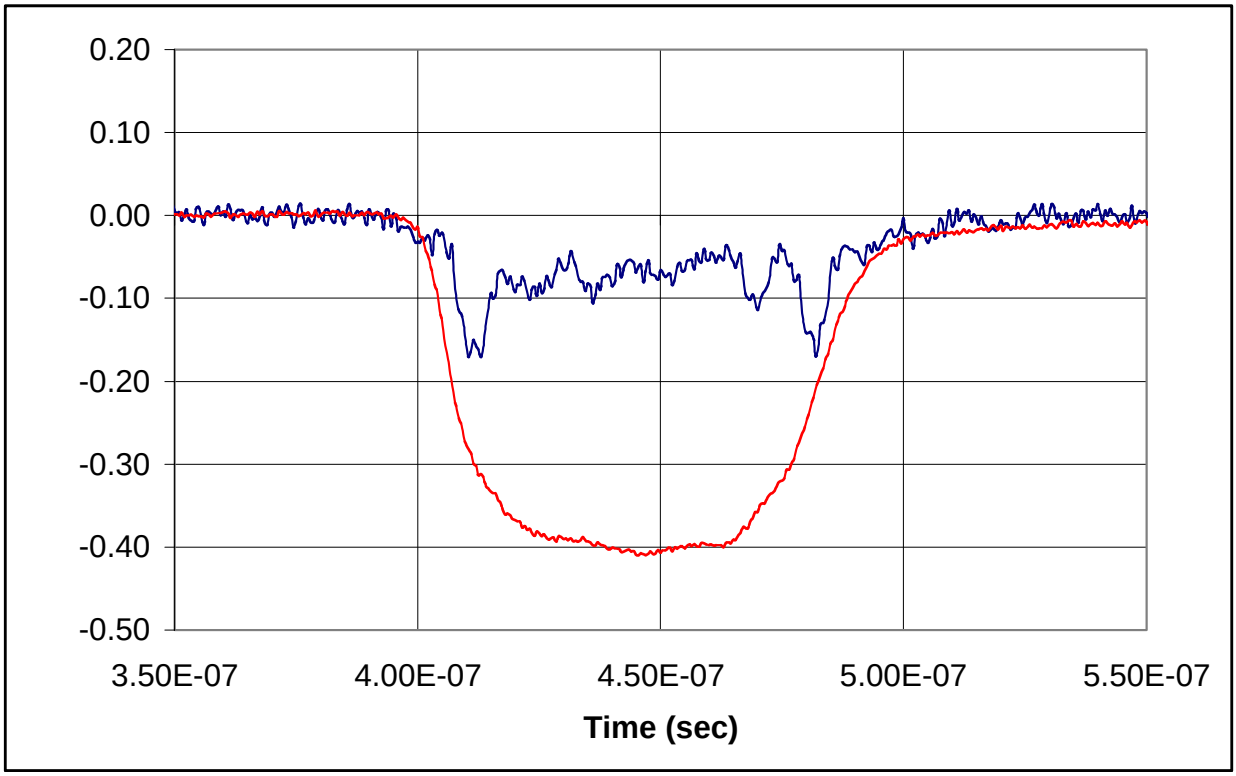

Figure D-4 The beam magnetic moment with scaled current overlay.

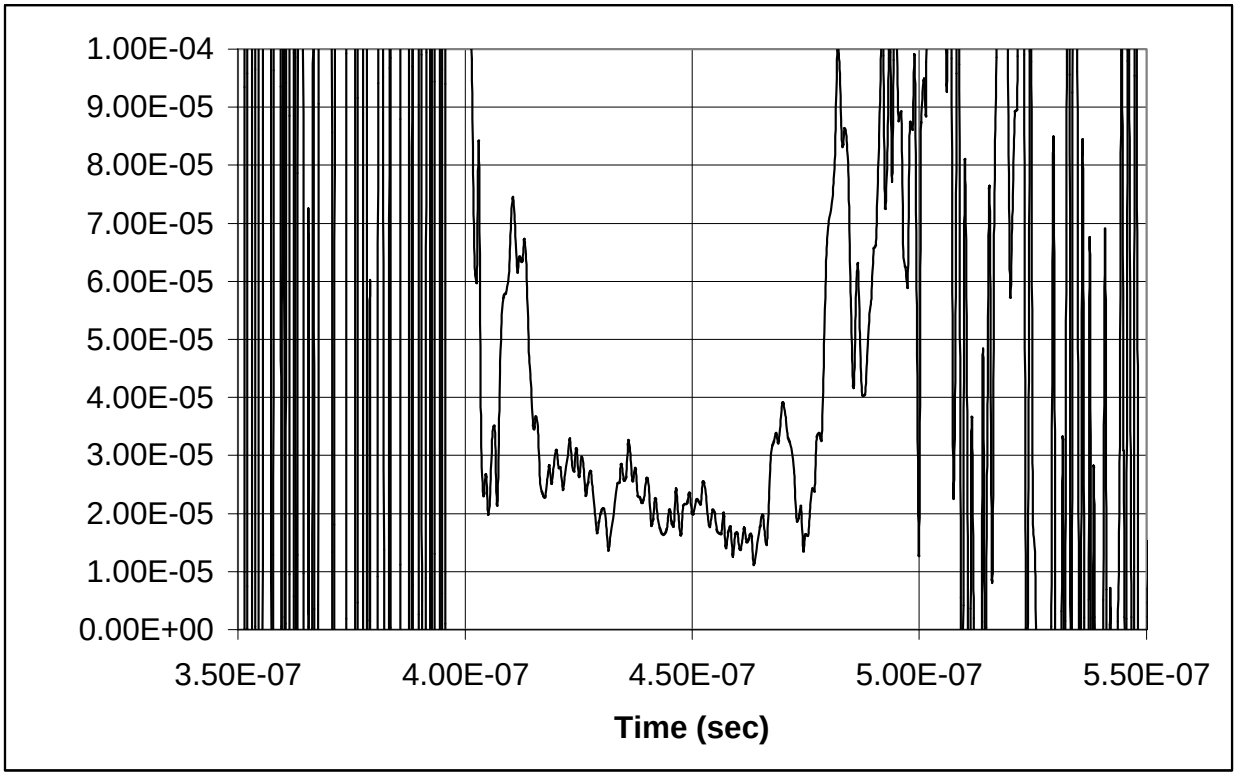

Figure D-5 Moment per unit current.

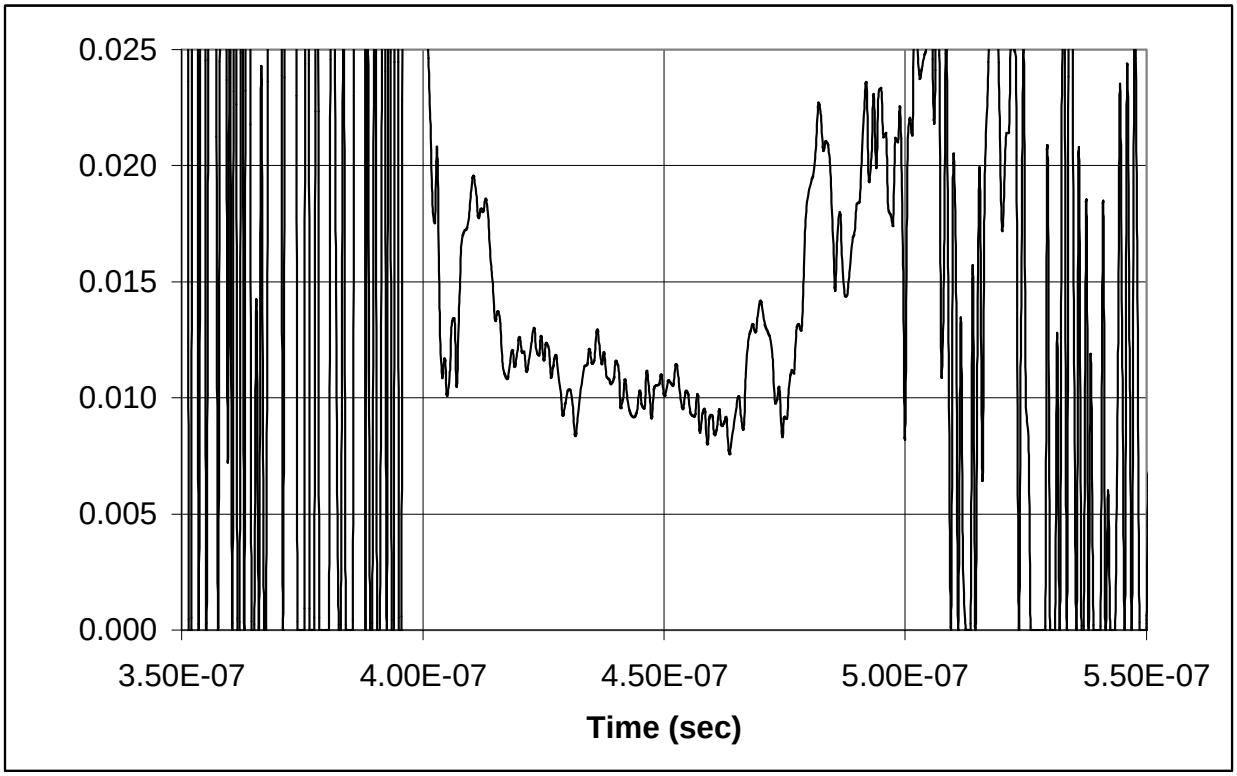

Figure D-6 Beam rms radius (γ = 34).

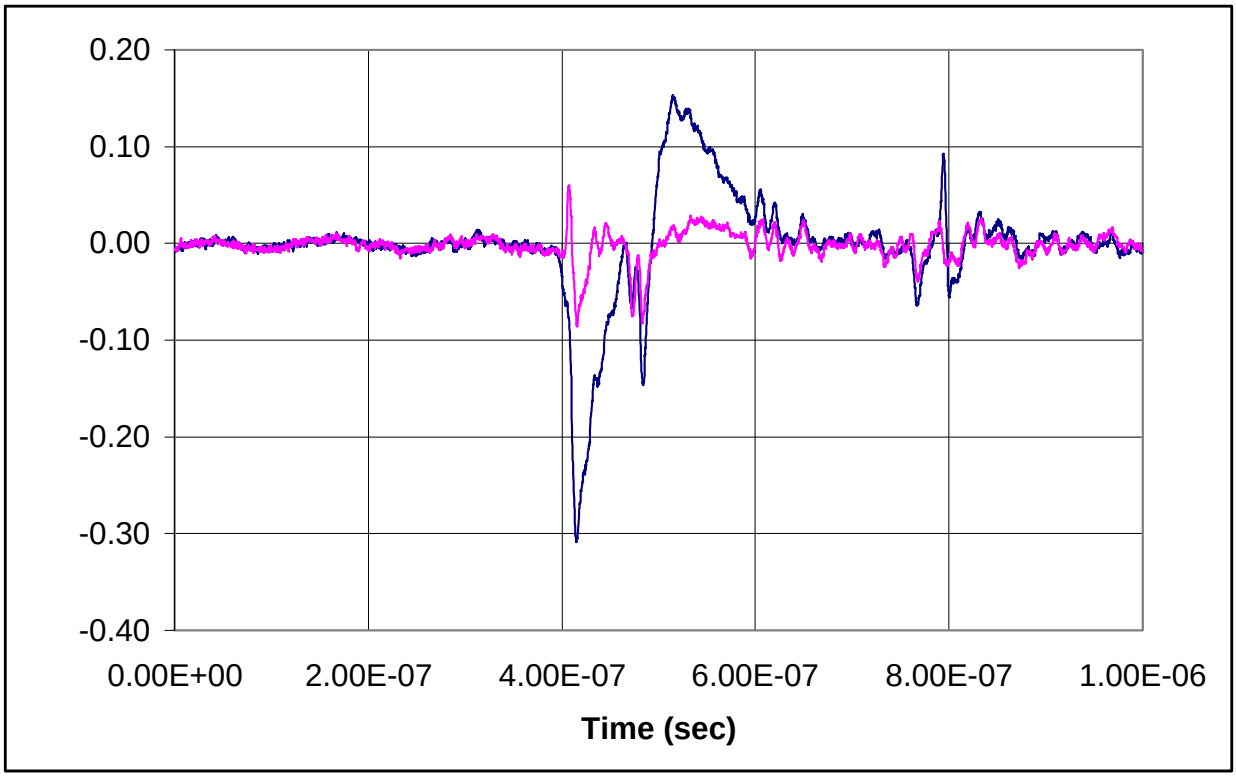

Figure D-7 Overlay of raw DML signals with and without loop field.

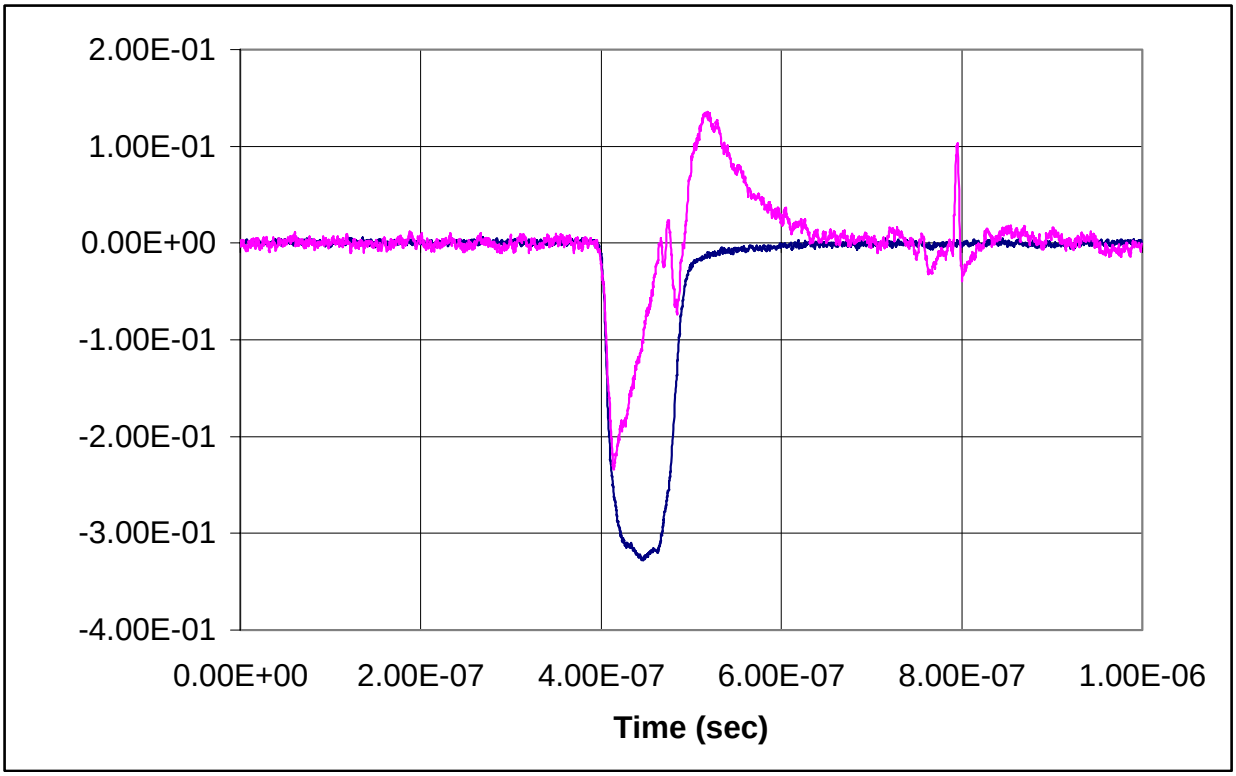

Figure D-8. Difference of D-7 signals. Scaled current overlaid.

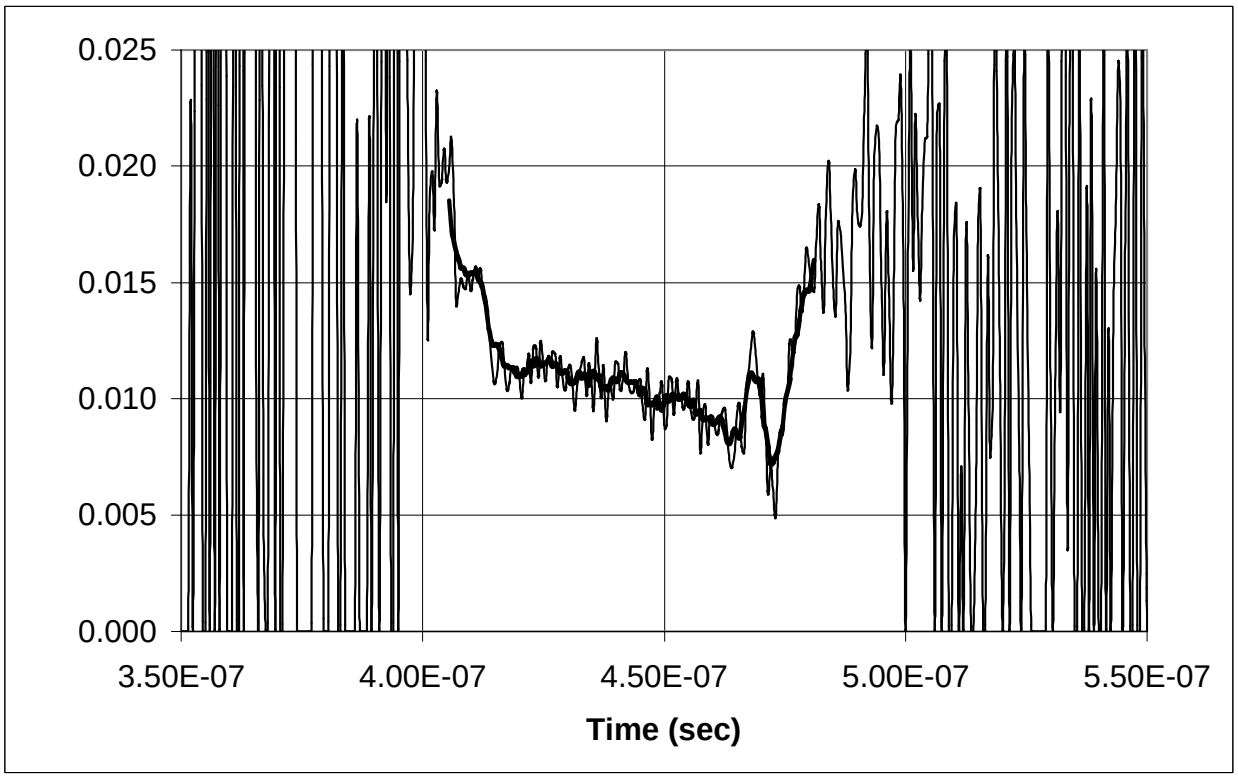

Figure D-9. Beam rms radius from data of Figure D-8. Smoothed radius overlay.

In Figure D-7 we plot an overlay of the raw DML signal of the above shot and a consecutive shot with no DML field. For both of these the beam was less than 1 mm from the axis during the period of peak current but had excursions of almost a centimeter during the rise and fall of the signal.. Shown is the complete record although beam is present for only a small part of the record. It is obvious that there is some repeatable non-random noise signal probably due to the firing of the Marx generators and the charging of the Blumlein lines. If we take the difference of these two signals we obtain Figure D-8, an appreciably cleaner signal and if we then reduce this data we obtain the beam radius data of Figure D-9 where much of the structure of Figure D-7 during the period around the current maximum has been greatly reduced.

Data reduction requiring the differencing of two shots is very rare, occurring when one is pushing the present limits of the measurements, i.e., high energy and small radius. A larger radius beam is desirable in the drift region to minimize the final spot size. Since our signal increases as the squire of the radius, a tune that doubles or triples the beam radius will greatly increase our signal strength and should make such subtraction unnecessary,

APPENDIX E-BEAM RECONSTRUCTION

Assuming a mono-energetic, emittance dominated, round beam, Paul has described a method for "reconstructing" the beam envelope rms radius, r_0, the slope of the beam envelope, $r_0'=dr_0/dz$, and the paraxial ray equation "emittance", ε_r, at a chosen point from measurements of the beam radius downstream under three different conditions of transport between the two points.[E-1] He considered using a foil for the radius measurement and, while a minimum of three shots were required for a measurement, he showed that, because of shot-to-shot variation, it would be necessary to reduce many shots to obtain the desired accuracy.

DMLs can be used instead of a foil, however, and since they do not interfere with the beam, data can be taken simultaneously with any number of loops. In particular in the drift region at the exit of an induction linac, the data from an array of three downstream DMLs, separated by known transport conditions from the exit, can be used to reconstruct the time resolved values of the exit parameters for each beam pulse. Since the DML yields rms values of the radius, we will obtain rms values of the exit parameters that are useful in predicting spot size [E-2]. These exit parameters can be compared with code predictions by using the relationship between rms values and boundary values for a constant density, hard-edged beam.

Paul has further simplified his approach by invoking the symmetry properties of a round beam [E-3]. If $\boldsymbol{R}$ is the beam transport matrix between two points separated by an axial symmetric solenoid,

$$\begin{vmatrix} x \\ x' \\ y \\ y' \end{vmatrix} = \boldsymbol{R} \begin{vmatrix} x_0 \\ x_0' \\ y_0 \\ y_0' \end{vmatrix}, \tag{E-1}$$

the transport matrix can be written as the product of a focusing matrix followed by a rotation of angle $\theta=kL_S$ where $k = \frac{q}{mc}\frac{B_S}{\sqrt{\gamma^2-1}}$ and L_S is the solenoid length. On the boundary of an axial symmetric round beam we can ignore the rotation and work in a (r,r') vector space where

$$\begin{vmatrix} r \\ r' \end{vmatrix} = \boldsymbol{F} \begin{vmatrix} r_0 \\ r_0' \end{vmatrix} \tag{E-2}$$

and $\boldsymbol{F}$ is now the simple focusing matrix

$$\boldsymbol{F} = \begin{vmatrix} \cos\theta & k^{-1}\sin\theta \\ -k\sin\theta & \cos\theta \end{vmatrix} \tag{E-3}$$

Let $\boldsymbol{\sigma_0}$ be the matrix characterizing the ellipse bounding the beam in the r_0, r_0' phase space at the accelerator exit. Its elements are

$$\begin{aligned} a &\equiv (\sigma_{11})_0 \\ b &\equiv (\sigma_{12})_0 = (\sigma_{21})_0 \\ c &\equiv (\sigma_{22})_0 \end{aligned} \tag{E-4}$$

From the definition of the sigma matrix, the beam radius, the slope of the beam envelope, and the beam emittance at the exit are

$$r_0 = \sqrt{a}$$
$$r_0' = b/\sqrt{a} \qquad \text{(E-5)}$$
$$\varepsilon_r = \sqrt{ac - b^2}$$

The σ_J matrix characterizing the bounding ellipse at measurement location J downstream is related to the σ_0 by

$$\sigma_J = R_J \sigma_0 R^T_J \qquad \text{(E-6)}$$

and the measured values of radius are related to the exit values of (E-4) through the σ_{11} components of (E-6)

$$\begin{aligned} r_1^2 \equiv (\sigma_{11})_1 &= C_{11}\, a + C_{12}\, b + C_{13}\, c \\ r_2^2 \equiv (\sigma_{11})_2 &= C_{21}\, a + C_{22}\, b + C_{23}\, c \\ r_3^2 \equiv (\sigma_{11})_3 &= C_{31}\, a + C_{32}\, b + C_{33}\, c \end{aligned} \qquad \text{(E-7)}$$

where

$$\begin{aligned} C_{J1} &\equiv [R_{11}^2]_J \\ C_{J2} &\equiv 2[R_{11}\, R_{12}]_J \\ C_{J3} &\equiv [R_{12}^2]_J \end{aligned} \qquad \text{(E-8)}$$

Writing (E-7) in matrix notation and solving for the initial conditions gives

$$\begin{bmatrix} a \\ b \\ c \end{bmatrix} = C^{-1} \begin{bmatrix} r_1^2 \\ r_2^2 \\ r_3^2 \end{bmatrix} \qquad \text{(E-9)}$$

Thus, if we know the transport conditions of (E-8) between the exit and the down stream locations, beam radii measurement at three points will allow the reconstruction of the beam exit conditions using (E-9) and (E-5).

The FXR DML array consists of a loop located at the exit of the accelerator measuring r_1, a drift region of length, L_1, a second loop measuring r_2, followed by a solenoid of peak field, B_S and length L_S, a second drift region of length L_2, and a third loop measuring r_3. For this array, the transformation matrices are:

$$\begin{aligned} R_1 &= I \\ R_2 &= L_1 \\ R_3 &= L_2 F L_1 \end{aligned} \qquad \text{(E-10)}$$

The pertinent components for the array are given in Table E-1.

Table E-1

J	1	2	3
$(R_{11})_J$	1	1	$\cos\theta - L_2 k \sin\theta$
$(R_{12})_J$	0	L_1	$(L_1 + L_2)\cos\theta + (k^{-1} - L_1 L_2 k)\sin\theta$

Substituting the values for the first two measurements and dropping the index on the third we find

$$C = \begin{bmatrix} 1 & 0 & 0 \\ 1 & 2L_1 & L_1^2 \\ R_{11}^2 & 2R_{11}R_{12} & R_{12}^2 \end{bmatrix} \qquad \text{(E-11)}$$

and

$$\boldsymbol{C}^{-1} = \frac{1}{D}\begin{vmatrix} D & 0 & 0 \\ L_1^2 R_{11}^2 - R_{12}^2 & R_{12}^2 & -L_1^2 \\ 2R_{11}R_{12} - 2L_1 R_{11}^2 & -2R_{11}R_{12} & 2L_1 \end{vmatrix} \qquad \text{(E-12)}$$

with

$$D = 2L_1 R_{12}^2 - 2L_1^2 R_{11} R_{12}$$
$$R_{11} = \cos\theta - L_2 k_s \sin\theta$$
$$R_{12} = (L_1 + L_2)\cos\theta + (k_s^{-1} - L_1 L_2 k_s)\sin\theta$$

where $k_s = \frac{q}{2mc}\frac{B_s}{\sqrt{\gamma^2 - 1}}$, $\theta = k_S L_S$, B_S and L_S are the solenoid field strength and length.

From (E-9) and (E-12) we find

$$a = r_1^2$$
$$b = \frac{1}{D}\left[(L_1^2 R_{11}^2 - R_{12}^2)\, r_1^2 + R_{12}^2\, r_2^2 - L_1^2\, r_3^2\right] \qquad \text{(E-13)}$$
$$c = \frac{1}{D}\left[(2R_{11}R_{12} - 2L_1 R_{11}^2)\, r_1^2 - 2R_{11}R_{12}\, r_2^2 + 2L_1\, r_3^2\right]$$

(While the matrix notation can greatly simplify the above presentation, the algebraic expressions of (E-13) are easier to incorporate into a spreadsheet when there are a large number of time steps to solve.)

A common assumption in code calculations is that all of the beam particles are within a constant density, hard edged beam of radius R, for which case $\langle r^2 \rangle = R^2/2$. We adopt this assumption, setting $R^2 = 2\langle r^2 \rangle$ in an attempt to reconcile DML measurements with those made by other methods and with code results. With this assumption it is likely that of the order of 90% of the beam particles lie within the boundary radius. From (E-5) it follows that

$$R_0 = \sqrt{2a}$$
$$R_0' = \sqrt{2}\, b / \sqrt{a} \qquad \text{(E-14)}$$
$$\varepsilon = 2\sqrt{ac - b^2}$$

E-1 Arthur C. Paul, "Reconstruction of Initial Beam Conditions at the Exit of the DARHT II Accelerator", UCRL-ID-137926 (February 18, 2000)

E-2 Yu-Jiuan Chen, "Final Focus Spot Size in a Solenoid Focusing System", UCRL-ID-152620 [April 8, 2003].

E-3 Arthur C. Paul. Private Communication.

APPENDIX F- ALTERNATIVE DML CONFIGURATIONS

My original DML design incorporated a loop of diameter smaller than the beam tube and mounted coaxially within the latter. This approach has the potential advantage of generating much larger signals, especially if mounted on a cantilever so as to be located under the peak magnetic field. It had the disadvantages, at least in my mind, of requiring very close mounting and alignment tolerances to avoid coupling into the azimuthal component of the beam magnetic field, and of being exposed to potential beam bombardment. Consequently I soon adopted the approach of adapting the existing beam bugs to include the loops, with the advantages and disadvantages outlined in the main section of this report.

Loops have been configured both as unbalanced with one lead internally grounded to the beam bug or balanced with two signal leads either floating or with the loop center point internally grounded to the beam-bug case. The signal of the unbalanced configuration had a large noise component that at the time was blamed on the internal grounding but in retrospect may have been due at least partially to electron bombardment. In almost all of the operation with the balanced configuration, a limited number of data channels made it necessary to use a hybrid coupler to difference the two loop signals, effectively hiding any common mode signal. Occasionally we would look at the common mode component but not enough to recognize what was happening until recently, when the luxury of additional data channels allowed us to dispense with the hybrid coupler and record both channels.

In the balanced mode configuration with the loop floating,the twisted leads are normally brought out radially through a small hole axially centered in the ferrite core. (During passage of

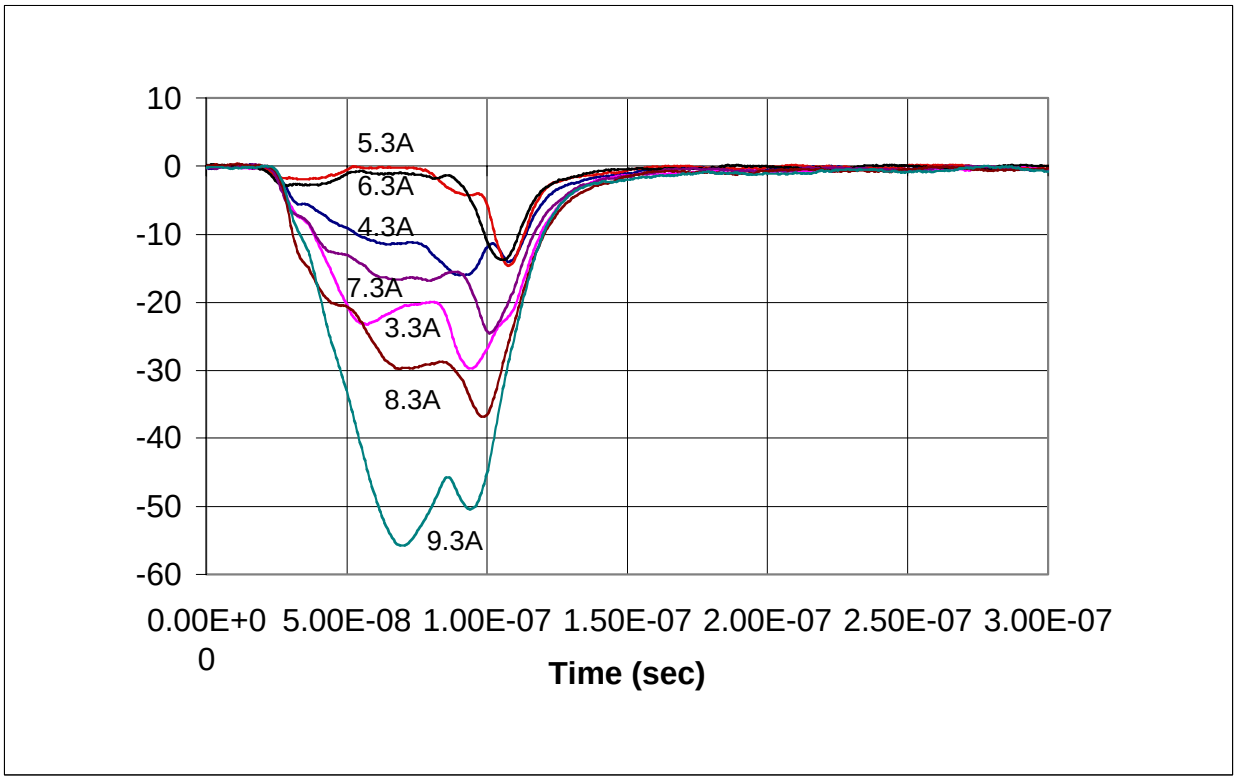

Figure F-1 Raw common mode signal. Upstream magnet current varied, zero field at loop.

the beam the axial voltage drop across the foil can be as high as 40 volts but by routing the leads in this manner the voltage difference between the loop and the midplane of the foil is kept low, thus avoiding spurious signals from currents charging the parasitic capacitance between the loop and the foil.) The two leads are connected to a pair of 50 ohm cables, time matched to a small fraction of a nanosecond, which conduct the signal from the accelerator vault to where they are recorded. It was not recognized for a long time that the loop was sensitive to bombardment by low-density electrons in the beam halo. In Figure F-1 with the field at the loop set to zero, the common mode signals are shown as the next upstream coil current is varied, thus changing the beam size at the loop. (Note that the signals go through a minimum as the upstream magnet current is raised.) The signals, which are quite repeatable, show a net electron current flowing into the loop whose value and time variation are controlled by the upstream field. Whether this current is due to secondary electrons produced by the energetic electrons striking the loop vicinity or whether an intermediate stage involving production of X-rays followed by Compton electrons is not known.We were sucessful in eliminating this signal by grounding the center-point of the loop winding but at the expense of introducing damped oscillations during the rise and fall of the beam current. This is demonstrated in Figure F-2 where the largest signal from

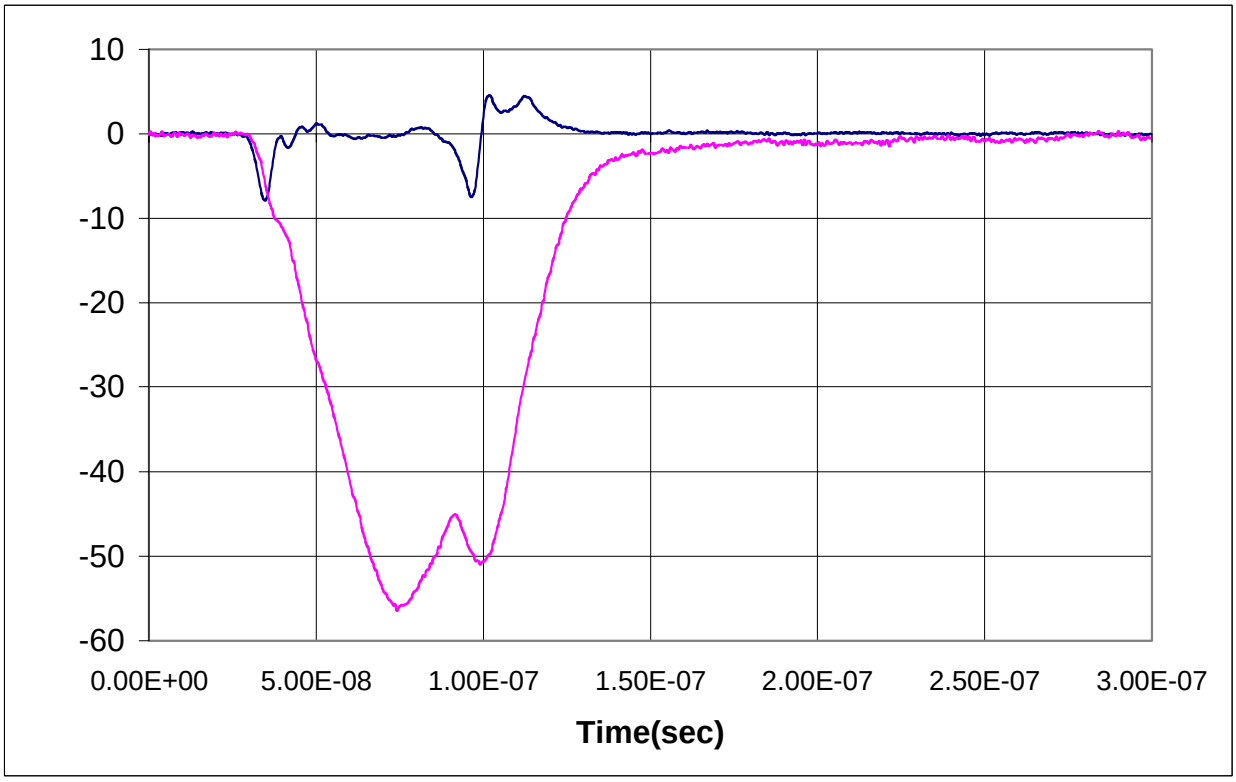

Figure F-2. Comparing signals from normal and center-point grounded loop under similar conditions.

Figure F-1 is overlaid with the signal obtained under similar operating conditions from the center-point grounded loop. The oscillations occur because in the present version the signal and ground leads were both brought around the same side of the core rather than through the hole bored in the core and as a consequence about half of the voltage drop across the foil is capacitivly coupled to the loop which resembles a quarter-wave strip-line structure. (If the ground lead had been threaded through the hole with the signal leads, it would not function as a

ground for frequencies of interest because of the impedence introduced by the ferrite. If the ground was routed around the core while the signal leads passed through the hole, the resulting loop would link half of the flux induced in the core by the beam current, resulting in a large common mode signal.) Both ungrounded and center–point grounded balanced loops can be used for moment measurements but there is room for improvement. One approach to further reduce the remaining common mode signal would be to route the center-point ground as at present, but run the twisted leads through the hole in the ferrite then around the half of the ferrite cross section opposite to the grounded side and through the hole again and on to the output connections. The resultant two turns each link half the core flux in a manner such as to eliminate or at least greatly reduce any contribution to the common mode signal due to the beam induced flux in the core and such a winding pattern should produce a large impedence in series with the load resistors to any net current flowing along the leads. Such an approach should result in the best DML data.

Before pursuing such changes which eliminate or greatly reduce the common mode signal one should decide whether one needs it to monitor beam bombardment of the wall. If so the original balanced floating loop configuration should be used and if it is found that the common mode signal is large with respect to the diamagnetic signal the loop signals should be fed into a 180^0 hybrid coupler which outputs the sum and difference of the two signals. The use of the hybrid coupler will allow the recording of the sum and difference signals, each with optimum gain but one must be aware that hybrids can not be interchanged without affecting the loop calibration and that they introduce some loss of sensitivity.

There is not enough radial space to mount our DML design directly under a solenoid, consequently they have been located adjacent to a solenoid and operated in bias fields in the range of 150-450 gauss. While these values have been adequate, higher fields do lead to better signal to noise ratios. If given the freedom to choose the DML location in a drift region, you should mount it upstream and as close as mechanically possible to one of the solenoidal lenses. At this location the beam radius at the DML will be very insensitive to the strength of the solenoidal field whereas if located downstream of the solenoid, the radius at the DML will depend on the focusing field.